

Molecular Line Observations of the Small Protostellar Group L1251B

Jeong-Eun Lee^{1,2}, James Di Francesco³, Tyler L. Bourke⁴, Neal J. Evans II⁵, Jingwen Wu⁴,

ABSTRACT

We present molecular line observations of L1251B, a small group of pre- and protostellar objects, and its immediate environment in the dense C¹⁸O core L1251E. These data are complementary to near-infrared, submillimeter and millimeter continuum observations reported by Lee et al. (2006, ApJ, 648, 491; Paper I). The single-dish data of L1251B described here show very complex kinematics including infall, rotation and outflow motions, and the interferometer data reveal these in greater detail. Interferometer data of N₂H⁺ 1–0 suggest a very rapidly rotating flattened envelope between two young stellar objects, IRS1 and IRS2. Also, interferometer data of CO 2–1 resolve the outflow associated with L1251B seen in single-dish maps into a few narrow and compact components. Furthermore, the high resolution data support recent theoretical studies of molecular depletions and enhancements that accompany the formation of protostars within dense cores. Beyond L1251B, single-dish data are also presented of a dense core located $\sim 150''$ to the east that, in Paper I, was detected at 850 μm but has no associated point sources at near- and mid-infrared wavelengths. The relative brightness between molecules, which have different chemical timescales, suggests it is less chemically evolved than L1251B. This core may be a site for future star formation, however, since line profiles of HCO⁺, CS, and HCN show asymmetry with a stronger blue peak, which is interpreted as an infall signature.

Subject headings: line: profile — ISM: individual (L1251B) — stars: formation

¹Department of Astronomy and Space Science, Sejong University, Seoul 143-747, Korea; jelee@sejong.ac.kr

²Hubble Fellow, Physics and Astronomy Department, The University of California at Los Angeles, PAB, 430 Portola Plaza, Box 951547, Los Angeles, CA 90095-1547

³National Research Council of Canada, Herzberg Institute of Astrophysics, 5071 West Saanich Road, Victoria, BC V9E 2E7, Canada; james.difrancesco@nrc-cnrc.gc.ca

⁴Smithsonian Astrophysical Observatory, 60 Garden Street, Cambridge, MA 02138; tbourke@cfa.harvard.edu

⁵Astronomy Department, The University of Texas at Austin, 1 University Station C1400, Austin, TX 78712-0259; nje@astro.as.utexas.edu, jingwen@astro.as.utexas.edu

1. INTRODUCTION

Most young stars in our Galaxy formed within groups or clusters (Lada and Lada 2003). Small, nearby groups of protostellar objects provide compelling cases for investigating the physical processes involved with such formation since the numbers involved are relatively small (e.g., $N < 10$) and the interactions of these objects with themselves and their environments are less complicated. For example, observational study of kinematics associated with young stars within groups and their immediate dense gas surroundings could provide evidence for a specific formation scenario, e.g., fragmentation or triggering, that is easier to see because of the simpler nature of groups relative to clusters.

Kinematic study of the gas surroundings of protostellar objects is achieved through observation and interpretation of molecular rotational transitions, since line profiles can be shaped by the motions within the source gas (see Di Francesco et al. 2006 for a review.) For example, outflow motions from young stellar objects were first seen in the low-intensity wings of CO 1–0 emission (e.g., Snell, Loren & Plambeck 1980). In addition, rotational motions in dense cores have been suggested from the detection of the shift of centroid velocities along different lines of sight in optically thin molecular transitions (e.g., Goodman et al. 1993). Finally, infall motions in dense cores have been the interpretation of profiles of moderately optically thick lines that are asymmetric with a stronger blue peak relative to optically thin lines (e.g., Zhou et al. 1993; Myers, Evans & Ohashi 2000). Such kinematic evidence has come primarily from single-dish telescopes, i.e., of relatively low spatial resolution, in studies of isolated protostellar objects. For protostellar groups, however, the surface density of objects can be high, and single-dish telescopes may not have the resolution needed to associate kinematics with particular protostars within the group. Instead, data from interferometers are very highly suited for such studies, especially when used in tandem with data from single-dish telescopes.

The use of molecular lines to study kinematics is complicated by potentially significant molecular abundance variations along the lines of sight toward dense gas both before and after star formation. Such abundance changes can be due to chemical evolution, intertwined with the YSO luminosity evolution since luminosity affects the temperatures of nearby dust grains that interact with gaseous molecules (see Rawlings & Yates 2001; Doty et al. 2002; Lee, Bergin & Evans 2004). Of course, YSO luminosity evolution is itself intertwined with dynamical evolution of the surrounding gas, as much of the luminosity originates from accretion. Hence, a holistic approach in general is required that includes luminosity, dynamics and chemistry, to understand best the environments from which stars form (see Bergin et al. 1997 and Aikawa et al. 2001 for early examples of such models).

Located at $300 \text{ pc} \pm 50 \text{ pc}$ (Kun & Prusti 1993), L1251B is an excellent example of

a small, nearby group of protostellar objects where molecular line observations can probe the kinematics and chemistry of its environment and yield clues about its origins. L1251B is located within L1251E, the densest C¹⁸O core in L1251 (Sato et al. 1994). L1251B is associated with a single IRAS point source, IRAS 22376+7455, and was found associated with CO outflow by Sato & Fukui (1989). In Lee et al. (2006; Paper I), we showed via single-dish data that IRAS 22376+7455 was associated with a local maximum of submillimeter emission, although significant peaks of 850 μm emission were also seen $\sim 150''$ to the east. In addition, we showed Spitzer Space Telescope (SST) observations of the region that revealed ~ 20 YSOs within $\sim 1 \text{ pc}^2$ covering L1251B and its surroundings, indicative of the formation of a group of low-mass stars. Within L1251B itself, these data revealed three Class 0/I objects (IRS1, IRS2, and IRS4) and three Class II objects (IRS3, IRS5, and IRS6), within a projected diameter of $55''$. (No near- or mid-infrared sources were found to be associated with other locations of submillimeter emission adjacent to L1251B.) Finally, we showed Submillimeter Array (SMA) continuum observations of L1251B in Paper I that revealed two compact locations of high column density between IRS1 and IRS2 that may be starless condensations. Paper I revealed clearly L1251B as a region of recent (and possibly continuing) star formation within a small group.

In this paper, we examine line emission associated with L1251B and the core $\sim 150''$ to its east (henceforth, the “east core”), to probe kinematic and chemical processes in the region. The three embedded Class 0/I sources and two starless objects within L1251B are especially emphasized; IRS1 is the most luminous object, IRS2 is located southeast of IRS1 and is associated with a near-infrared bipolar nebula, and IRS4 is located at the west of IRS1. The two starless objects are named as SMA-N (the northern one) and SMA-S (the southern one) in this paper. Besides the outflow noted by Sato & Fukui, earlier molecular line observations have also provided evidence for rotational and infall motions in L1251B. For example, a velocity gradient of $\sim 2.3 \text{ km s}^{-1} \text{ pc}^{-1}$ in the northeast–southwest direction across L1251B suggestive of rotational motion was detected by Goodman et al. (1993) in NH₃ (1,1) (also Sato et al. 1994; Tóth & Walmsley 1996; Anglada et al. 1997; Morata et al. 1997). In addition, infall motions toward L1251B were suggested from the detections of asymmetric profiles with stronger blue peaks in HCO⁺ 1–0 and 3–2, CS 2–1 and H₂CO 2₁₂–1₁₁ by Gregersen et al. (2000) and Mardones et al. (1997), though observations were published only toward the IRAS point source position. Since the relative intensity of a given molecular line depends upon distributions of density, temperature and molecular abundance along the line of sight, many other transitions and positions needed to be observed within L1251B and its surroundings to understand correctly their physical conditions and dynamical processes. Here, we have gathered with single-dish telescopes or interferometers new observations of L1251B in CS 2–1, 3–2, and 5–4, HCN 1–0, CO 2–1, ¹³CO 2–1, C¹⁸O 2–1, HCO⁺ 1–0

and 3–2, H^{13}CO^+ 1–0, DCO^+ 3–2, N_2H^+ 1–0 and H_2CO 3₁₂–2₁₁.

Details of the acquisition of observations of L1251B for this paper are summarized in §2. Results and analysis of the data are described in §3 and §4. In §5, we discuss the chemical and dynamical conditions in L1251B and the east core. Finally, a summary of the conclusions of this paper appears in §6.

2. OBSERVATIONS

2.1. The Five College Radio Astronomy Observatory (FCRAO) Observations

Observations of N_2H^+ 1–0 toward L1251B were made in December 1996 with the FCRAO 14-m telescope near New Salem, MA using QUARRY, the 15-element focal plane heterodyne receiver array. Observations of HCO^+ 1–0 and H^{13}CO^+ 1–0 were made toward L1251B also at FCRAO in April 1997 and May 2000, using the QUARRY (1997) and the 32-element SEQUOIA (2000) focal plane arrays respectively. The autocorrelator spectrometer was configured with a band width of 20 MHz over 1024 channels, providing a channel separation of ~ 20 kHz (~ 0.07 km s^{–1}). Typical system temperatures were 500–700 K (QUARRY) and 200–250 K (SEQUOIA). Observations of HCN J=1–0 and CS 2–1 toward L1251B were also made at FCRAO in February 2005 in OTF mode using SEQUOIA with a system temperature of ~ 120 K. A velocity resolution of 0.1 km s^{–1} was achieved with the 25 MHz band width on the dual channel correlator and the data were acquired in frequency-switching mode with an 8 MHz throw. The average pointing accuracy was about 4.5". Table 1 summarizes observational details of the FCRAO data, including the frequency (ν), velocity resolution (δv), the FWHM beam size (θ_{mb}), the main beam efficiency (η_{mb}), and the observing date for each line.

2.2. The Caltech Submillimeter Observatory (CSO) Observations

We observed the HCO^+ 3–2, CO 2–1, and DCO^+ 3–2 lines with the 10.4 m telescope of the CSO at Mauna Kea, HI in June 1997 and July 2003. HCO^+ 3–2 had been observed as part of the survey for infall signatures by Gregersen et al. (2000). We used an SIS receiver with an acousto-optic spectrometer (AOS) with a 50 MHz band width and 1024 channels. The frequency resolution was about 2 to 2.5 channels, i.e., ~ 0.13 km s^{–1} at 220 GHz. The pointing uncertainty was approximately 4" on average. Table 1 also summarizes observational details of these data.

2.3. The Caltech Owens Valley Radio Observatory (OVRO) Millimeter Array Observations

L1251B was observed in several transitions and continuum emission in the 1 mm or 3 mm bands of the OVRO Millimeter Array near Big Pine, CA over several observing seasons. The continuum data have been presented in Paper I. Table 2 summarizes the line data, i.e., the frequencies observed and the band widths used, as well as the velocity channel spacings, the synthesized beam FWHMs, and the 1σ rms values achieved.

In Fall 1997 and Spring 1998, $\text{H}_2\text{CO } J_{K-1K+1} = 3_{12}-2_{11}$ at 225.6977750 GHz (Pickett et al. 1998) was observed over 2 L-configuration and 1 H-configuration tracks for spatial frequency coverages of ~ 11 -156 k λ . These data were retrieved from the OVRO archive. In Fall 1998 and Spring 1999, $\text{HCO}^+ 1-0$ at 89.1885230 GHz (Pickett et al. 1998) was observed over 3 L-configuration tracks, for spatial frequency coverages of 4-35 k λ . These data were also retrieved from the OVRO archive. In Spring 2001 and Fall 2001, $\text{N}_2\text{H}^+ 1-0$ at 93.1762650 GHz¹ (Caselli, Myers & Thaddeus 1995) was observed over 5 L-configuration and 1 H-configuration tracks, for spatial frequency coverage of 4-64 k λ . These data were obtained specifically for this project. Refer to Paper I for details about observations and data processing.

2.4. The Submillimeter Array (SMA) Observations

L1251B was observed on 25 September 2005 from the summit of Mauna Kea, HI, with the Submillimeter Array (SMA) in its most compact configuration. The 230 GHz SMA receiver was tuned to observe $\text{CO } 2-1$, $^{13}\text{CO } 2-1$, $\text{C}^{18}\text{O } 2-1$, $\text{N}_2\text{D}^+ 3-2$, $\text{SO } 5_6-4_5$, and $\text{H}_2^{13}\text{CO } 3_{12}-2_{11}$ in separate correlator windows of various band widths and channel spacings. Table 3 lists the respective frequencies, sidebands of observation, correlator windows, band widths, and channel spacings for these lines. Out of the 24 windows in each sideband, the remaining correlator windows were used to observe continuum emission over effectively ~ 2 GHz in each sideband. The continuum data have been presented in Paper I. Refer to Paper I for general information on observations and data processing.

We used the MIRIAD software package for imaging and deconvolution. For the CO and ^{13}CO data, natural weighting was used without any tapering to make the respective

¹93.1762650 GHz is the frequency of the $\text{N}_2\text{H}^+ 101-012$ transition found by Caselli, Myers & Thaddeus (1995). The other 6 hyperfine components to the 1-0 transition, at frequencies < 6 MHz from that of 101-012 were also observed.

data cubes. The C^{18}O and N_2D^+ data, however, were tapered with a circular Gaussian of $4''$ FWHM during inversion to increase the beam size up to $\sim 5''$ FWHM for improved brightness sensitivity. Furthermore, only 20 velocity channels around the central velocity were used for the integrated intensity calculation to bring out low-brightness features. Finally, the SO and H_2^{13}CO data were tapered with Gaussians of $6''$ FWHM, also to improve brightness sensitivity, but no detections of either line were obtained. To calculate the integrated intensities, all channels were used with a 2σ rms clip.

2.5. Data from Other Observations

J. Williams (private communication) provided us with unpublished CS 3–2 and 5–4 data that were obtained with the NRAO 12-m telescope² on Kitt Peak, AZ in May 1996 (CS 5–4) and October 1997 (CS 3–2). The backend used was the Millimeter AutoCorrelator (MAC) with a channel spacing of ~ 48.8 kHz (~ 0.1 km s⁻¹ for CS 2–1 and ~ 0.06 km s⁻¹ for CS 5–4). Typical system temperatures were 250–300 K (CS 3–2) and 450–600 K (CS 5–4). Details of these line observations are also summarized in Table 1.

3. RESULTS

In this study, we use coordinates in the J2000 epoch, so the (α, δ) coordinates of IRAS 22376+7455, the IRAS point source associated with L1251B, are $(22^{\text{h}}38^{\text{m}}47.16^{\text{s}}, +75^{\circ}11'28.71'')$. This position defines the reference center for all figures that use offsets in their axes. For example, IRS1 is located at $(0'', +5'')$.

3.1. Observations with Single-Dish Telescopes

Figure 1 presents the integrated intensity maps of CS 2–1, HCN 1–0, HCO^+ 1–0 and N_2H^+ 1–0, obtained at FCRAO. In general, these lines trace moderately dense ($n \leq 3 \times 10^5$ cm⁻³) gas, i.e., they have low excitation requirements compared to other lines in this study. In each panel, line emission is shown overlaid onto a map of $850 \mu\text{m}$ continuum emission

²The Kitt Peak 12 Meter telescope was operated by NRAO, a facility of the National Science Foundation, operated under cooperative agreement by Associated Universities, Inc. It presently operated by the Arizona Radio Observatory (ARO), Steward Observatory, University of Arizona, with partial funding from the Research Corporation.

(see Paper I) and the locations of the YSOs IRS1, IRS2 and IRS4 are denoted by a circle, square and triangle respectively. Notably, the line maps of Figure 1 differ from the (low resolution) map of integrated CS 1–0 intensity by Morata et al. (1997), which instead shows a maximum of emission $\sim 200''$ north of L1251B and no obvious structure around L1251B itself. These line maps are similar to that of NH_3 integrated intensity by Tóth & Walmsley (1996), however. Figure 1 shows that L1251B is coincident with line emission maxima in all four tracers, suggesting it is associated with moderately dense gas. Significant line emission is also seen throughout the region beyond L1251B, however. For example, CS 2–1 shows a third maximum $\sim 130''$ north of L1251B, but no other tracer in Figure 1 shows a maximum towards that general location. In addition, other maxima are seen $\sim 100\text{--}160''$ to the east of L1251B, associated with the “east core” identified from $850\ \mu\text{m}$ emission in Paper I. These eastern maxima are not coincident with each other, however. Also, a thin ridge of emission extends northward from the east core in all maps. The brightnesses of the maxima are similar for CS 2–1, HCN 1–0, and H^{13}CO^+ 1–0 (not shown) in the east core and L1251B. The east core, however, is slightly brighter in HCO^+ 1–0 but much weaker in N_2H^+ 1–0 than L1251B, although it was not mapped as extensively in the latter line.

Figure 2 presents the integrated intensity maps of CS 3–2 and 5–4, HCO^+ 3–2 and DCO^+ 3–2 obtained with the NRAO 12-m telescope or the CSO. In general, these lines trace gas of higher density ($n \geq 1 \times 10^6\ \text{cm}^{-3}$) than those shown in Figure 1, i.e., they have relatively high excitation requirements. The maps of integrated intensity in Figure 2 are overlaid onto maps of 1.3 mm continuum emission, which traces the column density very well. (As described in Paper I, a shift in the location of the continuum emission maximum associated with L1251B to the south is seen with increasing wavelength.) The positions of IRS1, IRS2 and IRS4 are shown as in Figure 1, but here “square-X” symbols denote the locations the starless objects from Paper I, SMA-N and SMA-S. Figure 2 shows that L1251B also contains maxima of higher excitation lines, suggesting even higher densities than those traced by the lines shown in Figure 1. (These maps, however, do not extend as widely as those in Figure 1, so the larger-scale distribution of these lines, e.g., toward the east core, is not known.) As in the single-dish continuum data, however, Figure 2 also shows that the integrated intensity maxima of dense gas tracers are located consistently off-center from IRS1. For example, the maximum of CS 5–4 is located $\sim 15''$ (greater than a half beam size) south of IRS1. These shifts seen in continuum and molecular emission maps suggest that within L1251B the maximum column density, and probably the density, resides between IRS1 and IRS2.

Figure 3 shows line profiles at the center position of L1251B of all eight lines from Figures 1 and 2, plus H^{13}CO^+ 1–0. The line widths of DCO^+ 3–2, H^{13}CO^+ 1–0 and the isolated component of N_2H^+ 1–0, which are obtained by Gaussian fits, are $\sim 1\ \text{km s}^{-1}$. The

line widths of HCN 1–0 and N₂H⁺ 1–0, which are obtained by their hyperfine structure fits, are ~ 1.4 and ~ 1.2 km s⁻¹, respectively, probably affected by their optical depths. The width of CS 5–4, however, is ~ 2.6 km s⁻¹. Line wings are seen in the spectra of HCO⁺ 3–2, CS 5–4 and HCN 1–0. All profiles in Figure 3, except for H¹³CO⁺ 1–0, DCO⁺ 3–2, and the isolated component of N₂H⁺ 1–0 are asymmetric with blueshifted peak temperatures. The peak temperatures of the isolated component of N₂H⁺ 1–0 and DCO⁺ 3–2 lines are located close to the central velocity of L1251B, i.e., where the deepest dips are seen in the other lines. We determined the central velocities of L1251B (-3.65 km s⁻¹) and the east core (-4.13 km s⁻¹) by the Gaussian fitting of the isolated component of N₂H⁺ 1–0 and H¹³CO⁺ 1–0, respectively. Figure 4 shows profiles of five lines toward the east core, where again asymmetric profiles with stronger blue peaks are seen in HCO⁺ 1–0, CS 2–1, and HCN 1–0 but not H¹³CO 1–0. Such profiles are not seen everywhere across the region, however, indicating a complex velocity distribution. For example, the CS 2–1 line profile (not shown) has reversed asymmetry toward the northern maximum of CS 2–1. HCN 1–0 (not shown) also has a reversed profile between the east core and L1251B.

Figure 5a shows a map of red and blue components of CO 2–1 emission toward L1251B only, from data obtained with the CSO 10.4-m Telescope. The velocity ranges for the red and blue components of the outflow have been determined very conservatively from blue- and red-free spectra (Figure 5b).

The extended outflow from L1251B, as seen by others, is plainly noticeable. The projected orientation of the CO outflow is northwest–southeast with blue or red components respectively in the northwest or southeast. The two components overlap significantly at L1251B, however, and the origin of the outflow is not easily identifiable due to the low resolution of the map.

Figure 6 shows HCO⁺ 3–2 spectra from locations across L1251B. As seen in Figure 3, the central spectrum shows a very strong self-absorption dip and an asymmetric profile with a stronger blue peak. Figure 6 also reveals that the majority of lines off-center to L1251B have asymmetric profiles with stronger blue peaks, especially with increasing of the asymmetry with a stronger blue peak to the south. Not all the spectra are asymmetric with stronger blue peaks, however. To the north, the spectra are double-peaked more symmetrically, and in the north, reversed (red) asymmetry is seen. Note that the distribution of HCO⁺ integrated intensities at L1251B (Figure 2c) is elongated through the northwest–southeast direction. The outflow map (not shown) from the HCO⁺ 3–2 wing components seen in Figure 3 shows the same trend as seen in the CO 2–1 outflow map, i.e., a northwest–southeast extension and a significant positional overlap between the blue and red components.

3.2. Interferometric Observations

Figure 7 shows HCO^+ 1–0, N_2H^+ 1–0, and H_2CO 3_{12} – 2_{11} integrated intensities made with data from the OVRO MMA. Each map in Figure 7 is overlaid onto the *Spitzer* IRAC 4.5 μm band image, and the positions of IRS1, etc., are denoted as in Figures 1 and 2. In these cases, the maps only show smaller-scale emission features since significant flux on larger scales was resolved out by the interferometer. Figure 7 shows that the distributions of compact line emission differ significantly on small scales. For example, Figure 7a shows the HCO^+ 1–0 emission is elongated linearly in the northwest–southeast direction from IRS1, similar to the direction of the outflow seen on larger scales (see Figure 5). Figure 7a also shows that the N_2H^+ 1–0 emission is located between IRS1 and IRS2 and is elongated in a projected direction perpendicular to that of the HCO^+ emission. In contrast, Figure 7b shows compact H_2CO 3_{12} – 2_{11} emission in L1251B only at two locations, one centered at IRS1 and another 2'' to the northeast of IRS4.

Figure 8 shows maps of C^{18}O 2–1, N_2D^+ 3–2, CO 2–1, and ^{13}CO 2–1 integrated intensities from L1251B with data from the SMA. Again, the observations were sensitive to only small-scale, compact features. The distributions of compact line emission again differ remarkably from each other and from those shown in Figure 7. Figure 8a shows the C^{18}O 2–1 emission, along with N_2H^+ 1–0 emission shown previously in Figure 7a. Compact C^{18}O emission is found along a filament containing IRS1 and IRS2, as well as SMA-N and SMA-S. Some C^{18}O emission is also associated with IRS4. Note, however, that brighter C^{18}O emission is slightly offset from all objects in L1251B. N_2H^+ emission, however, is distributed in a direction perpendicular to the C^{18}O filament, but its maxima are more coincident with SMA-N and SMA-S (but not completely; see §4.4). In contrast, Figure 8b shows compact N_2D^+ 3–2 emission, which is detected in a single location, south of IRS1 and slightly offset to the west of SMA-S. Figures 8c and 8d show the compact CO 2–1 and ^{13}CO 2–1 emission, which both show a lobe-like structure extending southeast of IRS1. Bright CO emission is also seen to the northwest of IRS4, with a fainter extension coincident with IRS4. In contrast, bright ^{13}CO emission is coincident with IRS4 but is not seen to the northwest. Surprisingly, in these integrated intensity maps, neither CO nor ^{13}CO strong emission is seen associated with or coincident with IRS2, though its infrared nebulosity morphology is suggestive of an outflow cavity.

4. ANALYSIS

According to our observational results, complex dynamical and chemical processes are coupled in L1251B and the east core. To study each dynamical component, i.e., infall,

rotation, and outflow, in detail, we describe in this section the analysis of line profiles using line radiative transfer calculations and the simulation of observed line profiles (§4.1), centroid velocity maps and a position-velocity diagram (§4.2), and channel maps (§4.3), respectively. In addition, we calculate the chemical evolution coupled with the evolution of density and luminosity to compare the relative distribution of observed various molecular line emission with a chemical model (§4.4).

4.1. Infall

Toward L1251B, optically thick molecular transitions such as HCO^+ 1–0 and 3–2 show an asymmetrical profile with the brighter blue peak (see Figure 3). In addition, optically thin molecular transitions, such as H^{13}CO^+ 1-0 and DCO^+ 3-2 line are symmetrical, and peak at the velocities of the deepest dips of the other lines. Taken together, such profiles can be indicative of infall motions (see Zhou et al. 1993). In general, infalling gas will have motions both positive and negative along the line of sight, and if an excitation gradient exists also along line of the sight, redward self-absorption of gas emission can occur.

L1251B was modeled as an inside-out collapsing sphere (cf. Shu 1977) by Young et al. (2003), using continuum emission at $450\ \mu\text{m}$ and $850\ \mu\text{m}$ to find density and temperature profiles of the core. The model parameters provided by Young et al., however, do not correspond to the best-fit model (C. Young, personal communication). Instead, the infall radius of the actual best-fit collapse model of L1251B is 5000 AU, equivalent to an infall timescale of 5×10^4 years, rather than the 3000 AU provided by Young et al. Other parameters of the best-fit model are the same, i.e., an effective sound speed of $0.46\ \text{km s}^{-1}$ and a total luminosity of $10\ L_{\odot}$. The model with a 5000 AU infall radius provides much better SED fit. In the current best-fit model, the reduced χ^2 for intensity profiles at $450\ \mu\text{m}$ and $850\ \mu\text{m}$ and the SED are 17, 27, and 3, respectively (compare with χ^2 in Table 9 and 11 of Young et al.)

Figure 9 shows the density and velocity profiles of the best-fit inside-out collapse model. We have used the physical profiles to model HCO^+ 3–2/1–0, H^{13}CO^+ 1–0 and CS 5–4 lines with a Monte-Carlo radiative transfer code (Choi et al. 1995). These lines trace the densest region, i.e., where the infall velocity is significant, among the lines observed with single dish telescopes. To minimize a contribution from rotational motions, line profiles observed only at the core center have been modeled. The kinetic temperature profile (the dotted line in Figure 9a) has been calculated with a gas energetics code (Young et al. 2004; Doty & Neufeld 1997) from the dust temperature profile obtained from the dust continuum modeling. Abundance profiles of HCO^+ and CS were calculated with the chemo-dynamical model developed by

Lee et al. (2004). (This chemical calculation and its results will be described in §4.4.) Although an interferometric observation is necessary to study whether the high velocity wings of CS 5–4 are affected by outflow, Figure 10 shows that the density and infall velocity structures from the best-fit model of dust continuum observations can reproduce reasonably well the observed line profiles detected at the center of the core, especially CS 5–4. Note, however, that it was necessary to reduce the abundance profile of HCO^+ by a factor of 2 from that calculated by the chemical model, to fit the HCO^+ 3–2/1–0 line. The line profile of H^{13}CO^+ 1–0 was also fitted reasonably well with the HCO^+ abundance profile and the isotopic ratio of $^{12}\text{C}/^{13}\text{C} = 77$ (Wilson and Rood 1994). The dotted line in the Figure presents the comparison case without infall. In this model, constant turbulent widths of 0.6 km s^{-1} and 0.25 km s^{-1} (FWHM = 1 and 0.4 km s^{-1} , respectively) were assumed at radii respectively less than and greater than the infall radius. Having less turbulent motion in the outer stationary envelope than in the inner infalling envelope is necessary to fit the width of the self-absorption feature, especially that in HCO^+ 3–2. The broad line wings of HCO^+ 3–2/1–0 and H^{13}CO^+ 1–0, particularly pronounced in the blueshifted emission, are probably caused by outflowing material, which is not considered in this model. The higher ratio between blue and red peaks of the observed line profiles than the modeled ones, which is commonly seen and never understood, might be affected by the rotational motion or the non-spherical geometry.

4.2. Rotation

Beyond the central position of L1251B, variations of the line profiles and position-velocity diagrams suggest rotational motions. For example, the HCO^+ 3–2 line profiles shown in Figure 6 at positions offset from (0,0) show asymmetry reversals and increases that may be caused by rotational motions (e.g., see Walker et al. 1994; Zhou 1995; Ward-Thompson & Buckley 2001). A simulation of the HCO^+ 3–2 spectra with a 2-D Monte Carlo molecular line radiative transfer code (Hogerheijde & van der Tak 2000) for the collapse from a rotating dense cloud (Terebey, Shu & Cassen 1984) indeed produces the distribution of blue- and red-asymmetric profiles observed in L1251B (Lee et al., in preparation). Note, however, that the wings of line profiles along the projected outflow direction may be still affected by outflow motions (see §4.3 below).

Previous studies (Goodman et al. 1993; Sato et al. 1994; Tóth & Walmsley 1996; Anglada et al. 1997; Morata et al. 1997) determined that the overall velocity gradient in the L1251B neighborhood, i.e., that covered by the extended $850 \mu\text{m}$ map in Figure 1, was $\sim 1\text{-}2 \text{ km s}^{-1} \text{ pc}^{-1}$ in the northeast–southwest direction. Observations by Caselli et al. (2002),

however, revealed a more complex velocity distribution in the neighborhood, with gradients of opposite direction. Namely, L1251B itself is associated with a southwest–northeast gradient, while the east core is associated with a northeast–southwest gradient. The average direction reported in their paper, however, is also northeast–southwest, suggesting that the previous studies, with poorer resolutions, averaged out the velocity gradient associated with L1251B, whose velocity gradient is only about half of that in the east core. To determine the velocity gradient associated with L1251B and the east core at higher resolution, we fitted the hyperfine structures of HCN 1–0 and N₂H⁺ 1–0 and the Gaussian profile of H¹³CO⁺ 1–0, and found the same result as shown in Figure 6 of Caselli et al. For illustration, Figure 11 shows the centroid velocity distribution obtained from HCN 1–0, which shows different velocity gradients in L1251B and the east core. The derived velocity gradient from HCN 1–0 in L1251B within 80'' is $\sim 3/\cos(i)$ km s⁻¹ pc⁻¹ in the southwest–northeast direction but the velocity gradient in the east core is $\sim 6/\cos(i)$ km s⁻¹ pc⁻¹ in the opposite direction, i.e., consistent with the direction predicted from previous studies. Here, i is the inclination of the rotational axis from the plane of sky.

We have analyzed the centroid velocity shift in L1251B with the N₂H⁺ 1–0 interferometer data (see Figures 7a and 8a). Figure 12a shows a 2-D distribution of the mean centroid velocity with the integrated intensity contours of the isolated component of N₂H⁺ 1–0, which were calculated with the AIPS task, MOMNT. A clear shift of the centroid velocity is seen from the southwest to the northeast, along a direction perpendicular to the outflow direction. This southwest–northeast direction is *opposite* to directions of velocity gradient seen in previous studies with lower resolution but consistent with the result of Caselli et al. (2002) and that seen in HCN 1–0 (Figure 11) toward L1251B. A position-velocity diagram taken along a cut centered at (9'', -2'') and along P.A. = 33° (similar to the direction of maximum elongation of the N₂H⁺ emission) is seen in Figure 12b. The rotational motion suggested by this gradient is very fast, i.e., $30/\cos(i)$ km s⁻¹ pc⁻¹, $\Omega \sim 10^{-12}/\cos(i)$ s⁻¹ within 30''. This gradient is ~ 1 order of magnitude larger than what is seen on larger scales, such as in the HCN map (Fig. 11), suggesting an increased importance of rotation on small scales.

4.3. Outflow

In this section, we examine at high angular resolution the outflowing gas from the young stellar objects in L1251B, and provide an initial interpretation of the data. Although the evidence for outflows in this region is strong, the spatial distribution of this gas is very irregular, making it difficult to associate the observed outflow features with specific objects.

Figure 13 shows the CO 2–1 integrated intensity across L1251B as observed from the SMA, divided into red and blue components (emission at line center is excluded). For reference, the CO components are overlaid onto the 1.3 mm continuum emission across L1251B, also observed from the SMA. Figures 14 and 15 show channel maps of CO 2–1 respectively for red- and blueshifted emission. For reference, the CO emission in each channel is overlaid here onto the N_2H^+ 1-0 integrated intensity as observed from the OVRO millimeter array. (Note that the velocity range definitions of red- and blueshifted emission are slightly different in these Figures than those used for Figures 5 and 13 because of the difference in their velocity resolutions.) In Figures 14 and 15, we also include more channel maps at -1.2 km s^{-1} , and -5.4 and -6.5 km s^{-1} , in the red- and blueshifted emission, respectively, to resolve different outflow components. For an alternative view of the outflows associated with L1251B, Figure 16 shows channel maps of HCO^+ 1-0 observed from OVRO. In the channel maps, especially for blueshifted emission (Figure 15 and 16), velocities closer to the central velocity than defined conservatively in Figure 5 and 13 are covered. While the HCO^+ 1-0 emission around the central velocity peaks at SMA-S, which is the densest part in L1251B, at -5.2 and -5.6 km s^{-1} , it has peaks at IRS1 and southeast of IRS4 with a weaker tail toward the northwest of IRS4. Therefore, HCO^+ 1-0 mainly traces the outflowing material even at the velocity up to $\sim -5 \text{ km s}^{-1}$. In addition, the comparison between the model and observation of HCO^+ 1-0 in Figure 5b suggests that the emission at -5 km s^{-1} is affected only by the outflow.

As can be seen from Figure 13, significant outflow appears to be associated with IRS1. This emission, however, may also include a component from SMA-S. Bright emission is seen extending southeast of IRS1, with blueshifted emission to the east-southeast and redshifted emission to the south-southeast and some positional overlap of these components to the southeast. The overlap of the components could indicate a single outflow where the inclination of the axis from the plane of sky is not large and the blue and red components respectively trace the front and back components of an outflow cone. Note, however, that in the redshifted -1.2 km s^{-1} channel of Figure 14, the feature divides into two components, one associated to the west and southwest of IRS1 and another to the southwest of SMA-S. Note also the pair of distinct components seen in Figure 15, associated with IRS1 in one blueshifted pair of channels at -5.4 km s^{-1} and -6.5 km s^{-1} and associated with SMA-S in another blueshifted pair of channels at -9.6 km s^{-1} and -11 km s^{-1} . In the latter case, the emission may have been made compact and elongated in the northwest-southeast direction due to higher densities to its immediate northeast, as evident from the N_2H^+ emission and the higher-excitation line emission (see Figure 2).

For IRS2, a single redshifted feature is seen extending to its southeast in Figure 13, and this feature is also seen in the CO channel maps from 2 km s^{-1} to -1.2 km s^{-1} of Figure 14. No

corresponding blueshifted feature is obviously associated with IRS2, however. It is possible that the blueshifted feature near IRS1 seen at -5.4 km s^{-1} and -6.5 km s^{-1} is associated with IRS2 instead. For example, CO may be severely depleted in the dense regions between IRS1 and IRS2, and the blueshifted outflow from IRS2 may be only visible in CO near IRS1 because of localized high CO abundance due to the evaporation of CO from nearby dust grains. Note, however, that this blueshifted emission lies in a similar northwest-southeast direction as redshifted emission from IRS1. Alternatively, the extended redshifted feature southeast of IRS2 may be related to IRS1 itself.

Northwest of IRS4, Figure 13 shows red- and blueshifted features with very significant positional coincidence. Again, these features could be due to a single outflow of low inclination. The channel maps of Figure 14 and 15 suggest a more complex interpretation, however, with weak red- and blueshifted emission seen both northwest and east of IRS4 at -1.2 km s^{-1} , -5.4 km s^{-1} and -6.5 km s^{-1} . Figure 16 shows blueshifted emission from HCO^+ 1-0 also located to the east and the northwest of IRS4. Instead, there may be two outflows present, one centered at IRS4 and another to the northwest. This latter may originate from IRS1 and could be the counterpart to the redshifted emission seen southeast of IRS2. Note that not much material is seen between IRS4 and IRS1, in the continuum emission maps of Figures 2 and 9 or the CO 2–1 channel maps of Figure 13. Compact HCO^+ 1–0 emission *is* seen between IRS4 and IRS1, however, in Figure 16 from -6 km s^{-1} to -5 km s^{-1} . The strongest HCO^+ emission is seen southeast of IRS4, and this may constitute a blueshifted outflow component from IRS4.

A summary of the possible outflows in the L1251B region is shown in Figure 17, with outflow components schematically plotted over the 1.3 mm continuum emission observed with the SMA. In this picture, IRS1, IRS2, IRS4 and even SMA-S all have outflows, some of which interact with each other. If SMA-S indeed has an outflow, it is not a starless condensation after all. Instead, it may harbor a very low luminosity protostellar object that was undetected by Spitzer. The existence of such objects has been surmised by others; e.g., Rebull et al. (2007) suggested that several objects unseen at $\lambda < 70 \mu\text{m}$ could be driving numerous outflows observed in HH 211. Future observations of L1251B, at even higher resolutions or using various lines that clearly trace gas shocked by outflow motions (e.g., mid-infrared lines of H_2 or millimeter lines of SiO), will be very helpful in disentangling the association of the outflows with specific sources and their effects on the evolution of the L1251B core.

4.4. Chemistry

Within L1251B, our high-resolution maps provide continued evidence for the expected chemical behavior of dense gas not associated with protostars. For example, the HCO^+ features shown in Figure 7a likely traces outflowing dense gas, since HCO^+ can be made abundant through shocks (see Rawlings et al. 2004). As with HCO^+ , the CO, ^{13}CO , and diffuse C^{18}O emission seen in Figures 8a, c and d may also be due to extensive depletion in the extended envelope and enhancements along the outflow axis due to liberation from grains. Emission from these lines indeed share some common features, but note that no compact CO, ^{13}CO , or C^{18}O emission is seen between IRS1 and IRS4. A faint ridge of HCO^+ 1–0 emission is seen at that location in the level of 2σ , however.

In addition, the N_2H^+ feature shown in Figure 7a likely traces non-outflowing gas, since N_2H^+ can remain abundant in cold dense material and can be depleted significantly in outflows. N_2H^+ is a chemical daughter of N_2 , which forms slowly. The interactions between N_2H^+ and grains replenish N_2 in the gas phase because N_2H^+ recombines with electrons on the grain surfaces. The principal destroyers of N_2H^+ in the gas phase are CO and electrons. CO can be significantly depleted in starless cores (Bergin & Langer 1997) because the only source of heating is the interstellar radiation field and the inner temperatures of such cores can be correspondingly very low (e.g., ~ 7 K; see Evans et al. 2001). Also, the electron abundance can be very low ($\sim 10^{-9}$, Williams et al. 1998) in dense gas that is highly extinguished, like that in starless cores. The N_2H^+ emission seen in Figure 7a and 8a is consistent with the 1.3 mm dust continuum emission mapped by the IRAM 30-m Telescope (see Paper I), suggesting it is also tracing cold, dense gas.

N_2H^+ (and N_2D^+) will also deplete at densities greater than 10^6 cm^{-3} (Di Francesco, André & Myers 2004; Pagani et al. 2005). Note that the two N_2H^+ intensity maxima in Figure 7a and 8a are offset slightly to the east from SMA-N and SMA-S, which trace the densest parts of L1251B. (The C^{18}O emission observed with the SMA does not have maxima at SMA-N and SMA-S either.) In addition, an N_2D^+ emission maximum is found between IRS1 and SMA-S. Finally, no such emission is associated with SMA-N. The offset of the N_2H^+ maxima and deficiencies of N_2D^+ from these objects are possibly caused by the depletion from the gas phase at densities greater than 10^6 cm^{-3} . The N_2D^+ emission may be identifying a less dense location that has a high enough temperature to populate significantly N_2D^+ at $J=3$. For example, the $J=3$ level of N_2D^+ has its maximum population in thermal equilibrium at ~ 20 K, and this may be caused by heating by IRS1. (Note, however, that the temperature there cannot be greater than 30 K, because otherwise CO would evaporate off dust grains and reduce the N_2D^+ abundance.)

Our high-resolution observations of L1251B show further examples of the chemical be-

havior expected in the presence of nearby protostellar heating. Once a protostar forms, the surrounding material is heated up to the CO evaporation temperature (~ 25 K in the case of bare SiO₂ dust grains). The desorbed CO destroys N₂H⁺, producing an N₂H⁺ emission “hole” around the central heating source, that is potentially observable with interferometers. Such holes may explain the lack of N₂H⁺ emission coincident with IRS1 and IRS2, as seen in Figures 7a and 8a. In contrast, the abundances of other molecules such as CS, H₂CO, and HCO⁺ can be enhanced due to protostellar heating resulting in the desorption of CO or the desorption of themselves off of dust grain mantles (Lee, Bergin & Evans 2004) as seen in Figure 7b. In L1251B, IRS1 is luminous enough to evaporate CO in its inner envelope. Similar N₂H⁺ emission holes have been seen toward NGC 1333 IRAS 4A (Di Francesco et al. 2001) and L483 (Jørgensen 2004).

Figure 18 shows the results of a chemical evolution model made specifically for L1251B to quantify the observed line emission distributions. For this model, we used the chemodynamical model developed by Lee et al. (2004). We updated the chemical network to include more recent results on the N₂H⁺ chemistry, however, including a new binding energy of N₂, which is the same as that of CO (Öberg et al. 2005), and new rates of dissociative recombination of N₂H⁺ with electrons (Geppert et al. 2004). We also increased the initial abundance of sulfur by a factor of 3 to fit the CS 5–4 line profile in Figure 10a. The initial abundances of other species are the same as those in Table 3 of Lee et al. (2004). For a dynamical model, we adopted the best-fit Shu inside-out collapse model to the dust continuum emission as described in §4.1. Although L1251B has several sources, only one internal luminosity source at the center of a spherically symmetric envelope was assumed in the model. Since IRS1 is the dominant luminosity source by a factor of ~ 10 , however (see Paper I), this model is a reasonable first approximation, especially for interpreting the single dish observations. For this model, the infall rate from the disk to central protostar was tuned appropriately to match the luminosity calculated by observations at the given timescale (Young & Evans 2005). In addition, the interstellar radiation field was assumed to be attenuated to $G_0 = 0.3$ for consistency with the dust continuum modeling. An outflow was not included.

We do not compare this chemical model with interferometric observations quantitatively since the density profile assumed in the 1-D model is not appropriate for the high resolution observations that reveal multiple sources. The chemical distribution close to the central source, however, is most sensitive to the temperature environment, so we can look for the effects of temperature increases around IRS1 on the chemical abundances. As seen in Figure 18, the model predicts a CO evaporation radius (which accordingly is also the N₂H⁺ depletion radius) of ~ 0.007 pc ($\sim 4''$), i.e., similar to the observed radius of the N₂H⁺ hole at a 2σ level of integrated intensity (see Figure 7a). Furthermore, the model predicts an H₂CO abundance

peak at a radius of ~ 0.003 pc ($\sim 2''$), similar to the radius of the H_2CO emission at the 2σ level of the integrated intensity (Figure 7b). A second H_2CO abundance peak seen in Figure 18 caused by CO evaporation does not affect significantly the H_2CO emission distribution likely because of the lower density and temperature of material at ~ 0.006 pc relative to material at ~ 0.003 pc associated with the inner abundance peak. Therefore, this simple model is in good agreement with our observations close to the central source, where infall is kinematically dominant, and chemistry mainly depends on the evaporation of molecules from grain surfaces by heating.

Near IRS4, the associated H_2CO emission may not be due to an increased abundance due to localized dust grain heating. That source may not be luminous enough to heat grains above the H_2CO evaporation temperature at a projected distance of 600 AU. The coincidence of the maxima of the integrated intensity of $\text{H}_2\text{CO } 3_{12}-2_{11}$ (see Figure 7b) to one of that of $\text{HCO}^+ 1-0$ (see Figure 7a) suggests a possible origin from shocked outflow material. Note that the H_2CO emission close to IRS4 lies at redshifted velocities of -1.5 km s $^{-1}$ to -3 km s $^{-1}$, and lies spatially at a full synthesized beam width ($2''$) northeast of IRS4.

5. DISCUSSION

5.1. L1251B

L1251B harbors a small group of starless and protostellar objects. Three of the latter are classified as Class 0/I candidates, which are associated with dense envelopes. The observations of molecular lines around L1251B have revealed active processes, either dynamical (infall, rotation and outflow) or chemical (depletion and enhancement).

The 1.3 mm dust continuum observations of L1251B with the SMA revealed two condensations (SMA-N and SMA-S) unassociated with any detected near-infrared source. (Note that SMA-S may contain a newly formed protostellar object if an outflow originates from it; see Figs. 14 and 15, and §4.3). Table 4 shows masses along the line of sight towards IRS1, IRS2, SMA-N and SMA-S, determined using the peak intensities of the 1.3 mm image and assuming a dust temperature of 20 K. We determined masses along the lines of sight rather than total masses from the respective fluxes because the extents of each were difficult to define with certainty in the crowded field, especially for SMA-N and SMA-S. Furthermore, any differences in mass along the line of sight could be more easily discerned with a single sampling. Table 4 shows that the peak intensities are quite similar (i.e., within 50%), suggesting quite similar masses along the line of sight if the temperatures are common. If we assume for SMA-N and SMA-S a lower temperature of 10 K, which is more commonly

adopted for starless cores, their masses along the line of sight are greater than those for 20 K (and IRS1 and IRS2) by a factor of ~ 3 .

Given their designations as protostars, the fluxes of IRS1 and IRS2 likely include emission from their respective disk components. In particular, IRS2 is not resolved at the $\sim 4''$ resolution of the data, which is equivalent to a ~ 1200 AU linear distance at the 300 pc distance of L1251B. Since these sources are also highly embedded, however, the 1.3 mm fluxes also likely contain emission from their inner envelopes. In contrast, the fluxes of SMA-N and SMA-S likely include emission only from envelopes since these sources are not seen if lower spatial frequencies (i.e., < 11 k λ) are excluded, as discussed in Paper I. To distinguish the disks of IRS1 and IRS2 (as well as a possible disk of SMA-S) associated with outflows (§4.3), observations with higher resolution are needed. Note that 1.3 mm continuum emission is not detected towards IRS4, suggesting that it is not associated with any disk or inner envelope that could be detected at our sensitivity and resolution.

All objects in L1251B possibly form by fragmentation during gravitational collapse (Boss 1997; Machida et al. 2005). Turbulent fragmentation seems unlikely since the lines observed toward L1251B are not so broad as to be considered dominated by turbulence. For example, tracers of very dense gas such as DCO⁺ 3–2, N₂H⁺ 1–0, and H¹³CO⁺ 1–0 have line widths of ~ 1 km s^{–1}, consistent with the infall velocity at $n \sim 10^6$ cm^{–3} in the best fit inside-out collapse model of L1251B. In addition, CS 5–4, which traces much higher densities ($n \geq 5 \times 10^6$ cm^{–3}), shows the broadest line width among all the high density tracers we observed toward L1251B, i.e., ~ 2.6 km s^{–1}. Indeed, our inside-out collapse model shows an infall velocity at 5×10^6 cm^{–3} of ~ 2 km s^{–1}. Also, the infall velocity profile this model fits the observed CS 5–4 and HCO⁺ 3–2 reasonably well, with constant turbulent widths of 0.6 km s^{–1} and 0.25 km s^{–1} at radii less than and greater than the infall radius respectively (see Figure 10a). The velocity dispersions implied from such widths are not much greater than the thermal velocity dispersion before collapse. (The dotted line in Figure 10 presents the case without the infall velocity structure.) Therefore, the dynamics of L1251B seem dominated by gravitational collapse, combined with rotation and outflows, rather than turbulent motions.

5.2. The East Core

The east core seen in Figure 1 at 850 μ m and in various molecular lines has a radius of about 0.1 pc. The 850 μ m emission shows several sub-cores inside a larger structure traced by molecular emission. This difference may be related to a bias towards imaging smaller-scale emission in the continuum data and related to high optical depths in the line

data. For the continuum data, the SCUBA observations were made by chopping onto the sky, effectively filtering out emission on angular scales greater than the $\sim 120''$ chop throw (see Di Francesco et al. 2007), i.e., those traced by the molecular line data. In addition, the $850\ \mu\text{m}$ continuum emission is very likely optically thin, tracing quite dense material within a molecular core. For the line data, the molecular emission (see Figure 1) may have high optical depths and the sub-cores may not be visible, despite the similarities between the densities these particular lines trace and the mean density of the sub-cores, i.e., $\sim 10^5\ \text{cm}^{-3}$. Differences in the positions of maximum integrated intensities between these lines may also be due to their relative (but high) optical depths. (To determine if the $\sim 3\times$ higher resolution of the $850\ \mu\text{m}$ map relative to the molecular line maps in Figure 1 contributed to the different appearance of the continuum and line maxima, we smoothed the $850\ \mu\text{m}$ map to a resolution similar to that of the line maps ($60''$). The smoothed $850\ \mu\text{m}$ map, however, still shows an emission hole near the maxima of the line maps.)

The low optical depth of the $850\ \mu\text{m}$ emission suggests that the much stronger continuum peak toward L1251B ($\sim 1\ \text{Jy beam}^{-1}$) relative to the east core ($\sim 0.2\ \text{Jy beam}^{-1}$) is indicative of a larger column density toward L1251B even if L1251B has been heated by internal sources. (Note that the $850\ \mu\text{m}$ emission peaks close to SMA-S, not toward IRS1, as seen in Figure 6 of Paper I) The $850\ \mu\text{m}$ fluxes of L1251B and the whole east core are similar, suggesting that their masses are also similar if their temperatures and dust opacities are themselves similar, i.e., $\sim 4\ \text{Jy}$ and $\sim 2\ M_{\odot}$ if $T = 20\ \text{K}$ and $\kappa_{1.3\text{mm}} = 0.02\ \text{cm}^2\ \text{g}^{-1}$ (Krügel & Siebenmorgen 1994). Since L1251B contains several YSOs but the east core does not, it is likely that L1251B is warmer than the east core, however. Continuum observations at multiple wavelengths and modeling are needed to determine better relative values of dust temperature.

Table 5 lists the integrated intensities of molecular lines observed toward the centers of L1251B and the east core. To probe for any relative chemical evolution in the two cores, we compare the relative integrated intensities of the 1–0 transitions of H^{13}CO^+ 1–0 and N_2H^+ , molecules found to be abundant respectively at earlier and later times in models of chemical evolution (e.g., Lee et al. 2003 and references therein). For H^{13}CO^+ 1–0, the integrated intensities of L1251B and the east core are similar (i.e., $\sim 1.3\ \text{K km s}^{-1}$ and $\sim 1.1\ \text{K km s}^{-1}$ respectively). For N_2H^+ , however, the integrated intensity towards L1251B is larger than that towards the east core by a factor of two (i.e., $\sim 4\ \text{K km s}^{-1}$ vs $\sim 2\ \text{K km s}^{-1}$ respectively). The relative integrated intensity ratio between these lines, i.e., ~ 6 for L1251B and ~ 3 for the east core, may be due to the relative chemical evolution, with L1251B being more chemically evolved. (Note that the difference in N_2H^+ abundance might be greater than the difference in the N_2H^+ 1–0 intensity due to the higher optical depth in L1251B.) Such differences in chemical evolution may result from differences in density since the chemical

timescale shortens at a higher density. In addition, H^{13}CO^+ and its isotopologue HCO^+ deplete significantly more than N_2H^+ in cold, dense environments such as in L1251B (except in the immediate vicinities of protostellar objects). Therefore, the higher ratio between the N_2H^+ and H^{13}CO^+ intensities in L1251B than in the east core (Figure 1) may be caused by a denser environment in L1251B.

Various lines toward the east core suggest infall motions. Therefore, the east core may be in earlier states of dynamical and chemical evolution than those of L1251B, and may harbor star formation in the future.

6. SUMMARY

L1251E, the densest C^{18}O core of L1251 (Sato et al. 1994), has been observed at various molecular line transitions with single-dish telescopes, and L1251B, the protostellar group in the C^{18}O core, has been observed with millimeter interferometers. We have compared these molecular line data to continuum data presented in Paper I to study this region of L1251 more comprehensively. Our results include:

1. L1251E contains at least two cores, one coincident with L1251B and an east core detected from $850\ \mu\text{m}$ continuum emission and various emission lines. The integrated intensities of these lines show primary maxima that are coincident with L1251B and other, secondary maxima associated with the east core which are non-coincident. No embedded sources have been detected in the *Spitzer* IRAC or MIPS bands toward the east core (Paper I), suggesting it is starless. Asymmetric profiles with stronger blue peaks have been detected toward the eastern core, however, that are suggestive of infall motions. The east core appears less dense and less chemically evolved than L1251B.

2. The large-scale outflow associated with L1251B has been mapped in CO 2–1 with the CSO. Red and blue components of the outflow overlap around the brightest protostar, IRS1, and the near-infrared bipolar nebula source, IRS2. The CO 2–1 and ^{13}CO 2–1 maps observed with the SMA resolve the outflow into a few components.

3. HCO^+ 3–2 line emission observed with the CSO across L1251B shows widespread line asymmetry that suggests infall motions towards the central group, with evidence for rotational or outflow motions from modifications of the line profiles at many off-center locations.

4. On a large scale, L1251B has a velocity gradient that is half the magnitude of that in the starless east core and is opposite in direction. Previous low-resolution observations

averaged the velocity gradients of both, causing rotational motions in the region to be misinterpreted.

5. HCO⁺ 1–0 line emission observed with the OVRO MMA is centered at IRS1 and distributed linearly along the northwest–southeast direction of the larger-scale outflow. In contrast, the N₂H⁺ 1–0 line emission also observed with the OVRO MMA is distributed between IRS1 and IRS2 (like the position of maximum brightness of the IRAM 1.3 mm continuum emission) and extended perpendicular to the outflow, i.e., along the southwest–northeast direction. A position-velocity diagram of N₂H⁺ 1–0 indicates very fast rotation in this flattened envelope, i.e., $\Omega \sim 10^{-12}/\cos(i) \text{ s}^{-1}$, where i is the inclination of the rotational axis from the plane of sky.

6. The maxima of N₂H⁺ 1–0 and N₂D⁺ 3–2 integrated intensity observed with the OVRO MMA and SMA are offset from locations of maximum continuum brightness from the two starless objects, which were newly detected at 1.3 mm with the SMA (Paper I). This offset may be due to reduction of N₂H⁺ and N₂D⁺ abundances at very high densities.

7. OVRO MMA and SMA observations reveal a lack of N₂H⁺ emission at IRS1 (i.e., a “hole”) but C¹⁸O and the H₂CO emission is coincident with IRS1. These results are consistent with a chemo-dynamical evolution model where a central protostar heats up surrounding material. In this model, CO and H₂CO are abundant close to the protostar where they are released into the gas phase from grain mantles, but N₂H⁺ has had its abundance sharply reduced since it is depleted by reactions with gas-phase CO.

Support for this study was provided by NASA through Hubble Fellowship grant HST-HF-01187 awarded by the Space Telescope Science Institute, which is operated by the Association of Universities for Research in Astronomy, Inc., for NASA, under contract NAS 5-26555. This work was also supported by NSF grant AST-0307350 to the University of Texas at Austin and by the State of Texas. We are very grateful to an anonymous referee for valuable comments. We thank Jonathan Williams for allowing us to use his unpublished molecular line data, and we also thank Chad Young for his help for the dust continuum modeling of L1251B. We are also very grateful to Anneila Sargent for providing us the opportunity to observe L1251B with the OVRO MMA.

REFERENCES

- Aikawa, Y., Ohashi, N., Inutsuka, S.-I., Herbst, E. & Takakuwa, S. 2001, ApJ, 552, 639
Anglada, G., Sepúlveda, I., & Gómez, J.F. 1997, A&AS, 121, 255

- Bergin, E.A. & Langer, W.D. 1997, *ApJ*, 486, 316
- Boss, A.P. 1997, *ApJ*, 483, 309
- Caselli, P., Benson, P. J., Myers, P. C., & Tafalla, M. 2002, *ApJ*, 572, 238
- Caselli, P., Myers, P. C., & Thaddeus P. 1995, *ApJ*, 455, L77
- Choi, M., Evans, N. J., II, Gregersen, E. M., & Wang, Y. 1995, *ApJ*, 448, 742
- Di Francesco, J., Myers, P. C., Wilner, D. J., Ohashi, N. & Mardones, D. 2001, *ApJ*, 562, 770
- Di Francesco, J., André, P., and Myers, P. C. 2004, *ApJ*, 617, 425
- Di Francesco, J., Evans, N.J., II, Caselli, P., Myers, P.C., Aikawa, Y., & Tafalla, M. 2006, in *Protostars and Planets V*, eds. B. Reipurth, D. Jewitt, & K. Kiel, (University of Arizona: Tucson), in press (astro-ph/0602379)
- Di Francesco, J., Johnstone, D., Kirk, H. M., MacKenzie, T. & Ledwosinska, E. 2007, *ApJS*, submitted.
- Doty, S.D. & Neufeld, D.A. 1997, 489, 122
- Doty, S.D., van Dishoeck, E.F., van der Tak, F.F.S., & Boonman, A.M.S. 2002, *A&A*, 389, 446
- Evans, N.J.II, Rawlings, J.M.C., Shirley, Y., & Mundy, L.G. 2001, *ApJ*, 557, 193
- Geppert, W. D., Thomas, R., Semaniak, J., Ehlerding, A., Millar, T., Österdahl, F., af Ugglas, M., Djurić, N., Paál, A., & Larsson, M. 2004, *ApJ*, 609, 459
- Goodman, A.A., Benson, P.J., Fuller, G.A., & Myers, P. 1993, *ApJ*, 406, 528
- Gregersen, E.M., Evans, N.J.,II, Mardones, D.M., & Myers, P.C. 2000, *ApJ*, 533, 440
- Hogerheijde, M.R. & van der Tak, F.F.S. 2000, *A&A*, 362, 697
- Jørgensen, J.K. 2004, 424, 589
- Kruegel, E. & Siebenmorgen, R. 1994, *A&A*, 288, 929
- Kun, M. & Prusti, T. 1993, *A&A*, 272, 235
- Lada, C.J. & Lada, E.A 2003, *ARA&A*, 41, 57
- Lee, J.-E., Evans, N.J.,II, Shirley, Y.L., & Tatematsu, K. 2003, *ApJ*, 583, 789
- Lee, J.-E., Bergin, E.A., & Evans, N.J.II 2004, *ApJ*, 617, 360
- Lee, J.-E., et al. 2006, *ApJ*, 648, 491
- Mardones, D., Myers, P. C., Tafalla, M., Wilner, D. J., Bachiller, R., Garay, G. 1997, *ApJ*, 489, 719

- Machida, M.N., Matsumoto, T., Hanawa, T., & Tomisaka, K. 2005, MNRAS, 362, 382
- Morata, O., Estalella, R., López, R., & Planesas, P. 1997, MNRAS, 292, 120 ApJ, 376, 618
275
- Myers, P. C., Evans, N. J., II, & Ohashi, N. 2000, in “Protostars and Planets IV,” eds. V. Mannings, A. P. Boss & S. S. Russell, (University of Arizona: Tucson), p. 217
- Öberg K. I., van Broekhuizen, F., Fraser, H. J., Bisschop, S. E., van Dishoeck, E. F., & Schlemmer, S. 2005, ApJ, 621, 33
- Pagani, L., Pardo, J.-R., Apponi, A. J., Bacmann, A. & Cabrit, S. 2005, A&A, 429, 181
- H. M. Pickett, R. L. Poynter, E. A. Cohen, M. L. Delitsky, J. C. Pearson, and H. S. P. Muller 1998, ”Submillimeter, Millimeter, and Microwave Spectral Line Catalog,” J. Quant. Spectrosc. & Rad. Transfer 60, 883-890
- Rawlings, J.M.C. & Yates, J.A., 2001, MNRAS, 326, 1423
- Rawlings, J.M.C., Redman, M. P., Keto, E. & Williams, D. A. 2004, MNRAS, 351, 1054
- Rebull, L. M., et al. 2007, ApJS, in press (astro-ph/0701711)
- Sato, F. & Fukui, Y. 1989, ApJ, 343, 773
- Sato, F., Mizuno, A., Nagahama, T., Onishi, T., Yonecura, Y., & Fukui, Y. 1994, 435, 279
- Shu, F.H. 1977, ApJ, 214, 488
- Shirley, Y.L., Evans, N.J.II, Rawlings, J.M.C. & Gregersen, E.M. 2000, ApJS, 131, 249
- Snell, R. L., Loren, R. B., & Plambeck, R. L. 1980, ApJ, 239, L17
- Terebey, S., Shu, F.H., & Cassen, P. 1984, ApJ, 286, 529
- Tóth, L.V. & Walmsley, C.M 1996, A&A, 311, 981
- Walker, C.K., Narayanan, G., & Boss, A.P. 1994, ApJ, 431, 767
- Ward-Thompson, D. & Buckley, H.D. 2001, MNRAS, 327, 955
- Williams, J.P, Bergin, E.A., Caselli, P., Myers, P.C., & Plume, R. 1998, ApJ, 503, 689
- Wilson, T.L. & Rood, R.T., 1944, ARAA, 32, 191
- Young, C.H., Shirley, Y.L., Evans, N.J.II, & Rawlings, J.M.C. 2003, ApJS, 145, 111
- Young, K.E., Lee, J.-E., Evans, N.J.,II, Goldsmith, P.F., & Doty, S.D. 2004, ApJ, 614, 252
- Young, C.H. & Evans, N.J.II 2005, ApJ, 627, 293
- Zhou, S., Evans, N.J.II, Koempe, C., & Walmsley, C.M 1993, 404, 232

Zhou, S. 1995, ApJ, 442, 685

Table 1. **Molecular line observations with single-dish telescopes**

Line	ν (GHz)	$\delta\nu$ (km s ⁻¹)	θ_{mb} (arcsec)	η_{mb}^a	Observing Dates	Observatory
H ¹³ CO ⁺ 1–0	86.754285	0.14	62	0.5	April 1997, May 2000	FCRAO
HCN 1 – 0	88.631847	0.10	61	0.5	February 2005	FCRAO
HCO ⁺ 1–0	89.188523	0.13	60	0.5	April 1997, May 2000	FCRAO
N ₂ H ⁺ 1–0	93.176265	0.13	58	0.5	December 1996	FCRAO
CS 2 – 1	97.980968	0.10	55	0.5	February 2005	FCRAO
DCO ⁺ 3 – 2	216.112605	0.13	34.7	0.74	July 2003	CSO
CO 2 – 1	230.53800	0.12	32.5	0.64	July 2003	CSO
HCO ⁺ 3–2	267.557526	0.12	22.5	0.67	June 1997, July 1998	CSO
CS 3 – 2	146.969048	0.10	43	0.8 ^b	October 1997	NRAO
CS 5 – 4	244.935606	0.12	26	0.5 ^b	May 1996	NRAO

^aThis main beam efficiency is used to convert the antenna temperature (T_a^*), only corrected for atmospheric attenuation, radiative loss and reward scattering and spillover, to the radiation temperature.

^bThese numbers represent the corrected main beam efficiencies (η_m^*) to convert the antenna temperature (T_R^*), corrected for forward scattering and spillover as well as atmospheric attenuation, radiative loss and reward scattering and spillover, to the radiation temperature.

Table 2. OVRO Observational Summary

Tracer	Transition	Bandwidth (MHz)	Channel Spacing (km s ⁻¹)	Gaussian Taper FWHM (" × ")	Synthesized Beam FWHM (" × ")	Synthesized Beam P.A. (°)	1 σ rms ^a (Jy beam ⁻¹)
H ₂ CO	3 ₁₂ -2 ₁₁	7.00	0.17	1.60 × 1.60	2.5 × 2.3	304	0.1
HCO ⁺	1-0	8.00	0.42	5.5 × 5.5	7.5 × 6.9	313	0.09
N ₂ H ⁺	1-0	7.50	0.20	4.0 × 4.0	6.5 × 5.2	334	0.07

^a1 σ rms computed from signal-free regions of the deconvolved maps.

Table 3. SMA Line Observations

Line	Freq. ^a (GHz)	S-band	Window	Chans	ΔV (km s ⁻¹)	Beam FWHM ("x ")	P.A. (degree)
CO 2–1	230.5380000	USB	14	128	1.06	4.1 × 3.1	-26.2
¹³ CO 2–1	220.3986765	LSB	13	512	0.26	4.3 × 3.4	-23.5
C ¹⁸ O 2–1	219.5603568	LSB	23	512	0.26	5.3 × 5.0 ^b	0.50
N ₂ D ⁺ 3–2	231.3216650	USB	23	512	0.26	5.1 × 5.0 ^b	10.4
SO 5 ₆ –4 ₅	219.9494420	LSB	18	256	0.53	8.0 × 6.3 ^{b,c}	68.3
H ₂ ¹³ CO 3 ₁₂ –2 ₁₁	219.9085250	LSB	19	256	0.53	8.0 × 6.3 ^{b,c}	68.3

^aAll line frequencies listed were obtained from Pickett et al. (1998)

^bBeam attained after tapering with a 4" × 4" FWHM Gaussian

^cBeam attained after tapering with a 6" × 6" FWHM Gaussian

Table 4. SMA 1.3 mm peak intensities and masses

Source	Peak Intensity, $I(\lambda)$ (Jy beam ⁻¹) ^a	Mass (M _⊙ beam ⁻¹) ^b
IRS1	0.035	0.031
IRS2	0.023	0.020
SMA-N	0.023	0.020 (0.055) ^c
SMA-S	0.029	0.026 (0.070) ^c

^aUncertainties on the peak intensities are 4 mJy beam⁻¹.

^bMasses have been calculated based on the equation,
 $Mass (M_{\odot} beam^{-1}) = \frac{I(\lambda) d^2}{\kappa_{\lambda} B_{\lambda}(T_{dust})} = 0.88 \times I(\lambda) (Jy beam^{-1})$ at
 $d = 300$ pc and $\lambda = 1.3$ mm, which is derived from the assumptions
of (1) the 1.3 mm opacity (κ_{λ}) of 2×10^{-2} cm² g⁻¹ (Kruegel &
Siebenmorgen 1994) and (2) the dust temperature (T_{dust}) of 20 K
for the Planck function, B_{λ} .

^cThe mass if $T_{dust} = 10$ K.

Table 5. Integrated Intensities of Molecular Lines (K km s^{-1})

Line	L1251B	East Core
HCO^+ 1–0	6.6	7.6
H^{13}CO^+ 1–0	1.3	1.1
CS 2–1	3.2	2.8
HCN 1–0	4.2 (4) ^a	3.0 (0.85) ^a
N_2H^+ 1–0	7.8 (2.2) ^a	3.8 (1.7) ^a

^aThe optical depth of the main component obtained by the hyperfine structure fit.

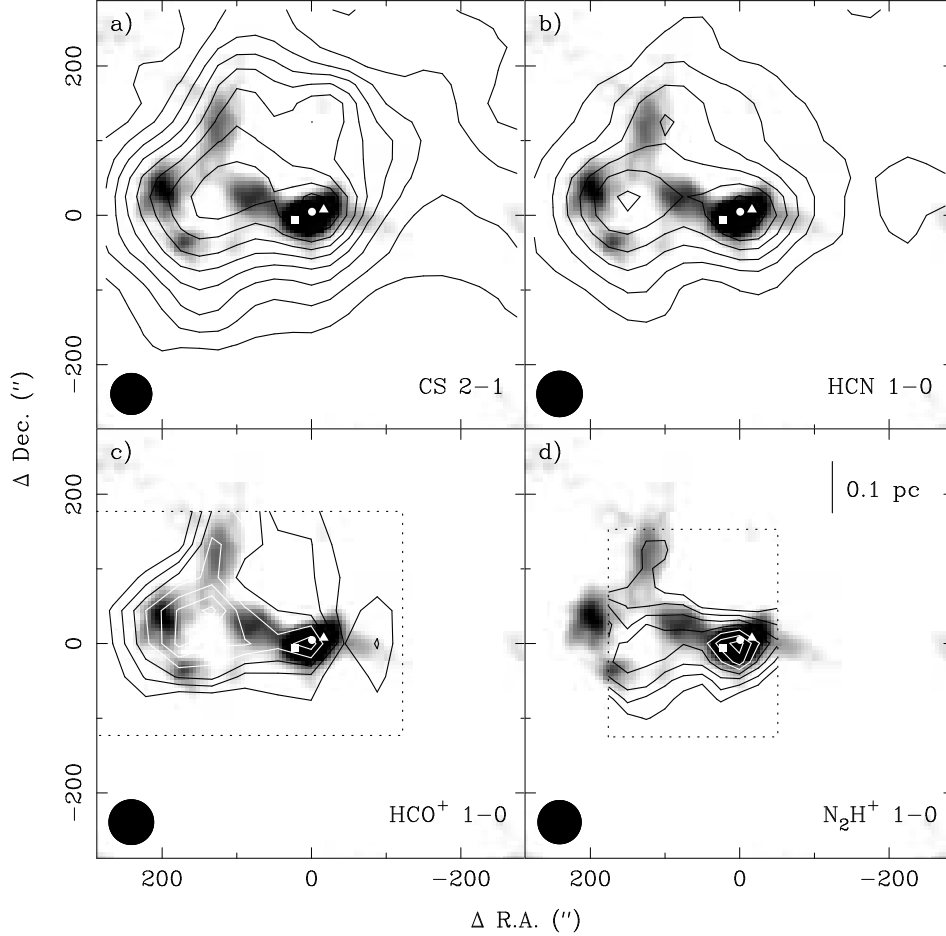


Fig. 1.— Integrated intensity maps (contours) of CS 2–1, HCN 1–0, HCO⁺ 1–0, and N₂H⁺ 1–0 on top of the 850 μ m emission map (grey scale). The (0,0) position of this map represents the coordinates of IRAS 22376+7455. In each panel, the small white circle, box and triangle denote the positions of IRS1, IRS2 and IRS4 respectively. In each panel, the grey scale used ranges from 0.084 to 0.420 Jy beam⁻¹, roughly 2 σ to 10 σ , where 1 σ \approx 0.042 Jy beam⁻¹. In each panel, the large black circle at lower left shows the beam FWHM. In each panel, the dotted rectangle shows the extent of the map in the respective line. (For CS 2–1 and HCN 1–0, the map was larger than the area shown.) a) Integrated intensity map of CS 2–1. The velocity range used is -6.5 to -0.5 km s⁻¹. The contours begin at 10 σ and increase by 6 σ where 1 σ = 0.06 K km s⁻¹. b) Integrated intensity map of HCN 1–0. The velocity range used is -13.5 to 4 km s⁻¹. The contours begin at 10 σ and increase in steps of 5 σ where 1 σ = 0.106 K km s⁻¹. c) Integrated intensity map of HCO⁺ 1–0. The velocity range used is -6 to -2 km s⁻¹. The contours begin at 6 σ and increase in steps of 1.5 σ where 1 σ = 0.42 K km s⁻¹. d) Integrated intensity map of N₂H⁺ 1–0. The velocity range used is -13 to 4 km s⁻¹. The contours begin at 15 σ and increase in steps of 5 σ where 1 σ = 0.166 K km s⁻¹.

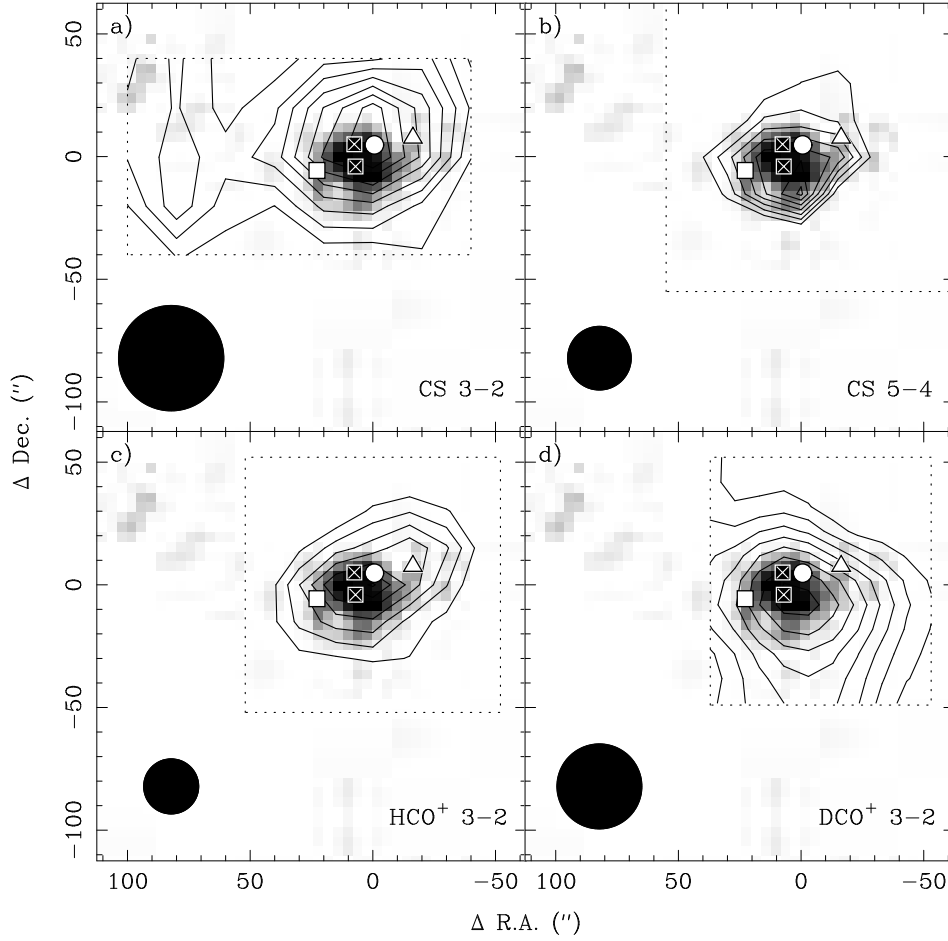


Fig. 2.— Integrated intensity maps (contours) of CS 3–2, 5–4, HCO⁺ 3–2, and DCO⁺ 3–2 on top of the 1.3 mm dust continuum emission map (grey scale). The grey scale ranges from 0.025 to 0.125 Jy beam⁻¹ or about 2 σ to 10 σ , where 1 σ = 0.0125 Jy beam⁻¹. In each panel, the dotted rectangle denotes the extent of the map in the respective line. Symbols are defined as in Figure 1 but here the square-X symbols indicate positions of peak intensity of prestellar condensations detected in SMA 1.3 mm observations (see Figure 8 of Paper I). a) Integrated intensity map of CS 3–2. The velocity range used is –6.5 to –0.5 km s⁻¹. The contours begin at 15 σ and increase in steps of 5 σ where 1 σ = 0.066 K km s⁻¹. b) Integrated intensity map of CS 5–4. The velocity range used is –6.5 to –0.5 km s⁻¹. The contours begin at 10 σ and increase in steps of 4 σ where 1 σ = 0.112 K km s⁻¹. c) Integrated intensity map of HCO⁺ 3–2. The velocity range used is –8 to 0 km s⁻¹. The contours begin at 3 σ and increase in steps of 3 σ where 1 σ = 0.545 K km s⁻¹. d) Integrated intensity map of DCO⁺ 3–2. The velocity range used is –5 to –2.5 km s⁻¹. The contours begin at 3 σ and increase in steps of 1 σ where 1 σ = 0.097 K km s⁻¹.

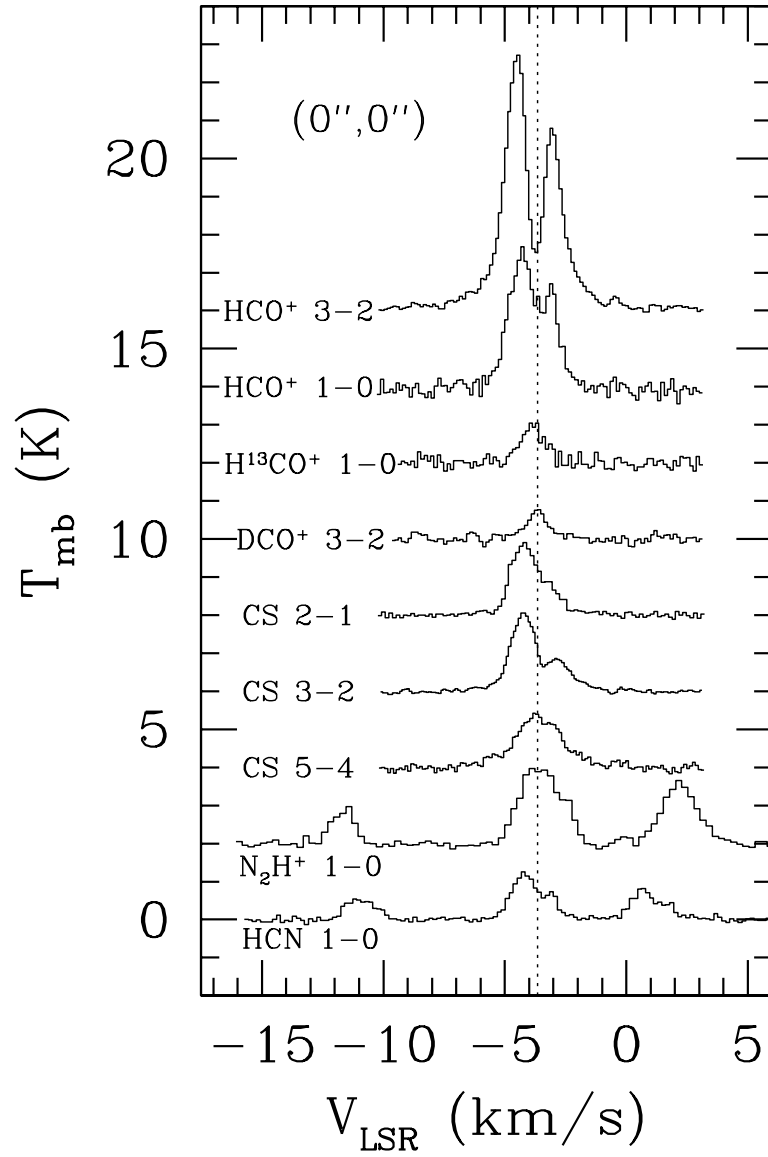


Fig. 3.— The spectra of all molecular transitions observed with single dish telescopes (Table 1) at the center position. To present line profiles better, the order of lines has been chosen arbitrarily, and spectra have been shifted up. The dotted vertical line indicates the centroid velocity of L1251B, -3.65 km s^{-1} .

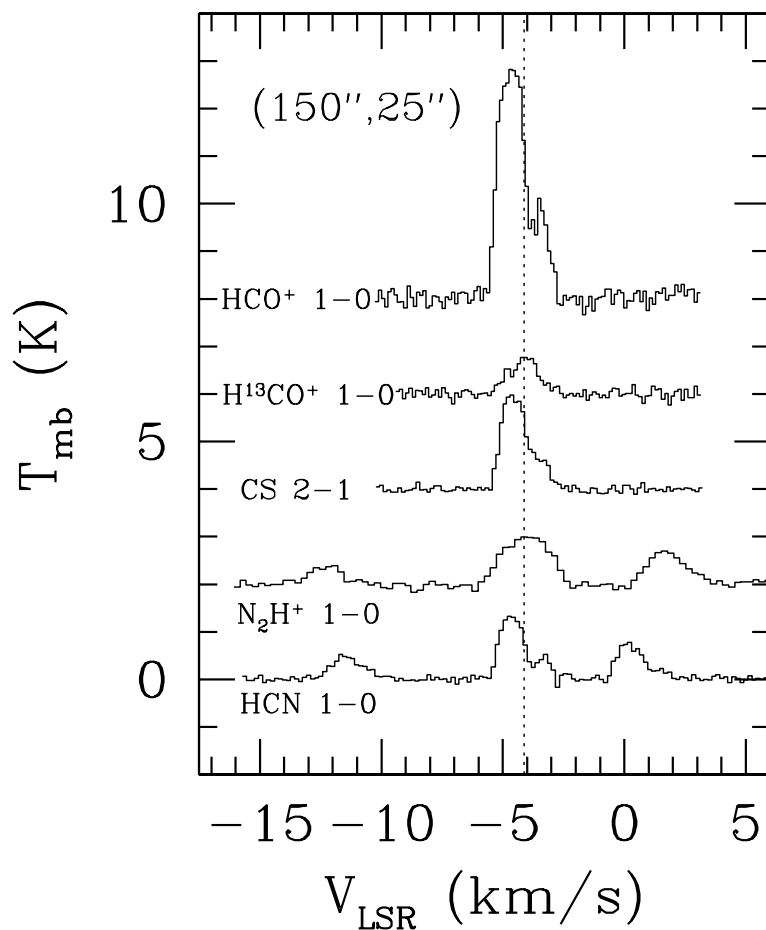


Fig. 4.— The spectra of some molecular transitions observed with single-dish telescopes toward the starless east core at $(150'', 25'')$. To present line profiles better, the order of lines has been chosen arbitrarily, and spectra have been shifted up. The dotted vertical line indicates the centroid velocity of the east core, -4.13 km s^{-1} which is derived from the Gaussian line fitting of $\text{H}^{13}\text{CO}^+ 1-0$.

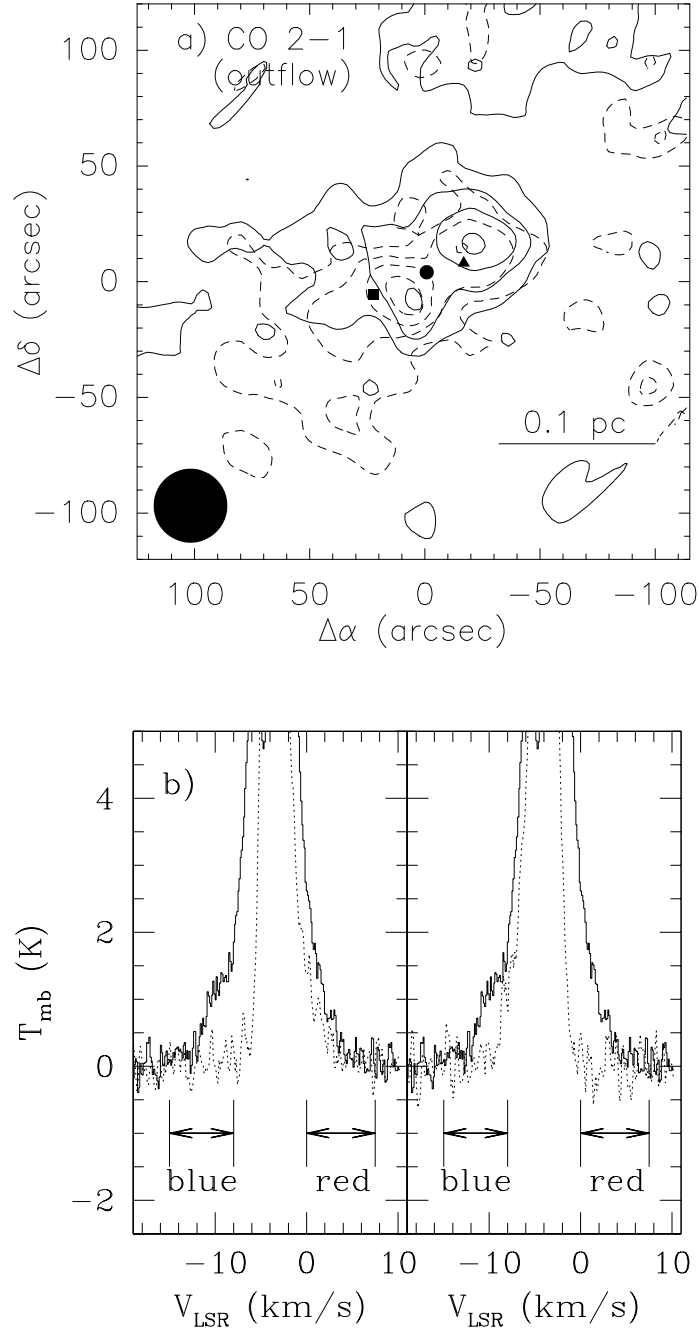


Fig. 5.— a) The distribution of the outflow in L1251B in CO 2–1. Symbols are defined as in Figure 1. The solid contours and dashed contours represent the blue and red components of the outflow, respectively. Contours are every 1 K km s^{-1} ($1 \sigma = 0.5 \text{ K km s}^{-1}$). The velocity range used for the blue and red components are -15 to -8 km s^{-1} and 0 to 7.5 km s^{-1} , respectively. b) The spectrum at the center compared with blue- (left) and red-free (right) spectra. Arrows indicate the velocity ranges for the blue and red components.

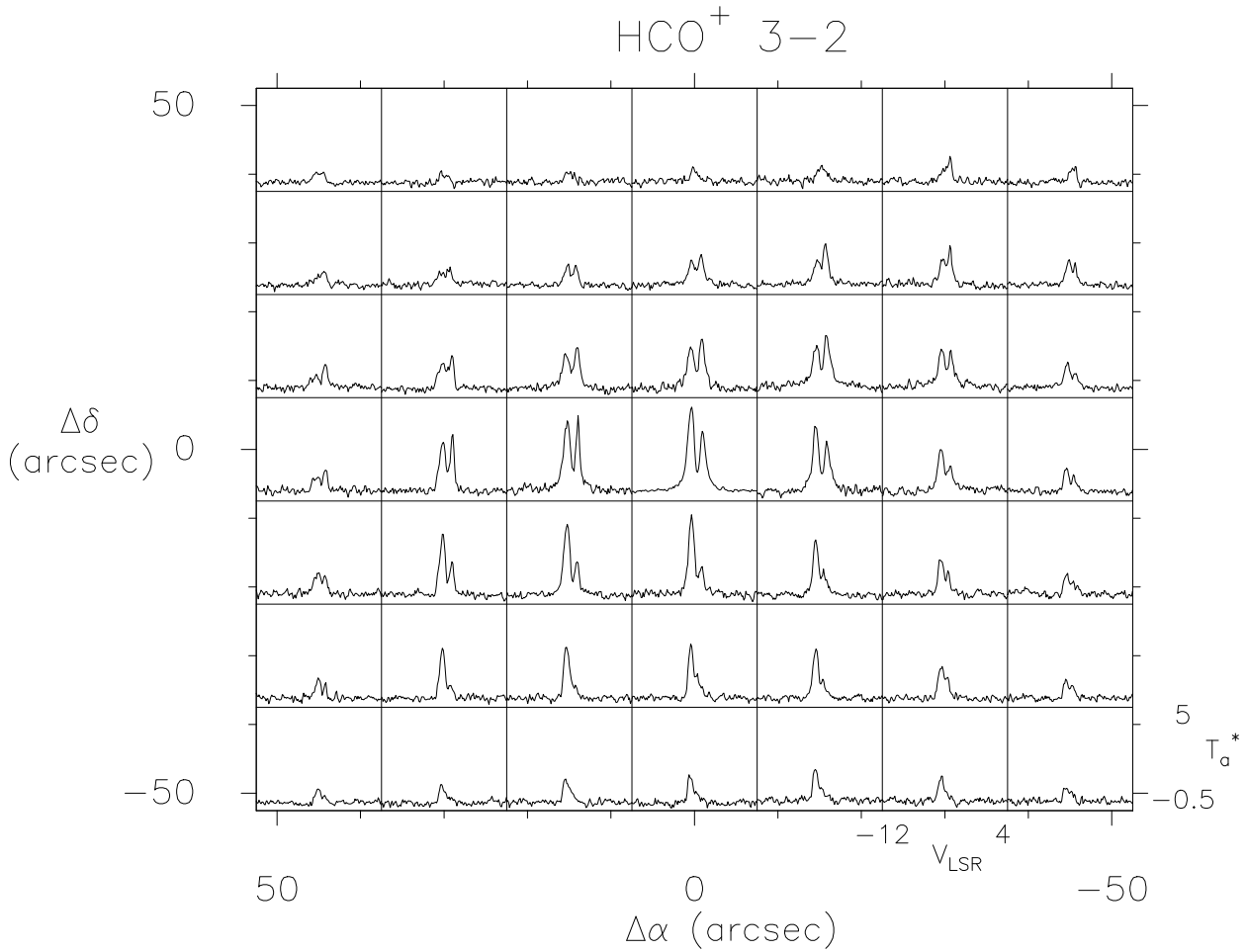


Fig. 6.— The spectra of $\text{HCO}^+ 3-2$ across L251B. Panels are spaced by $15''$ in R.A. and Dec. The horizontal axis is for V_{LSR} whose range is -12 km s^{-1} to 4 km s^{-1} , and the vertical axis is in T_a^* whose range is -0.5 K to 5 K .

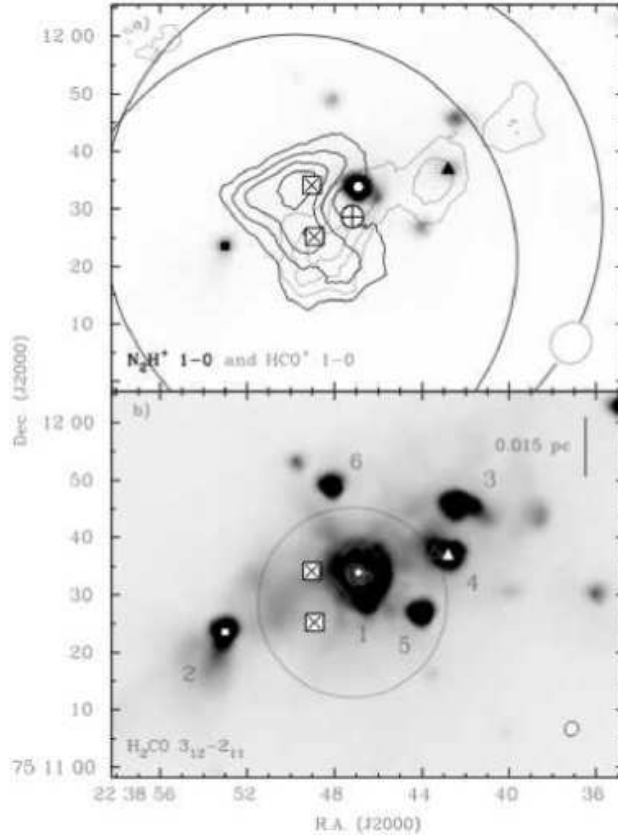


Fig. 7.— Integrated intensities of molecular transitions observed at OVRO, found by determining the “zeroth-moment,” i.e., summing over channels with emission $> |2| \sigma$. In all cases, no corrections for primary beam attenuation have been made. Each contour set begins at the respective 2σ level and increases in steps of the respective 2σ . Integrated intensities are overlaid onto an image of the same region as seen in IRAC Band 2 (inverted grey scale). In each panel, the ellipse to the lower right denotes the size and P.A. of the synthesized beam FWHM. Symbols are defined as in Figure 2, although the position of IRAS 22376+7455 is shown as a circle-cross symbol. a) N_2H^+ 1–0 (thick contours) and HCO^+ 1–0 (thin contours) where $1 \sigma = 1.5 \text{ K km s}^{-1}$ for N_2H^+ 1–0 and $1 \sigma = 1.3 \text{ K km s}^{-1}$ for HCO^+ 1–0. (The beam FWHM shown is that of the HCO^+ 1–0 data.) The outer large circle shows the FWHM of the primary beam of the HCO^+ data while the inner large circle shows the FWHM of the primary beam of the N_2H^+ data. For the IRAC Band 2 data, the grey scale range is -0.5 – 100 MJy sr^{-1} . b) Integrated intensities of H_2CO 3₁₂–2₁₁ (contours), where $1 \sigma = 0.54 \text{ K km s}^{-1}$. The large circle shows the FWHM of the primary beam of H_2CO data. For the IRAC Band 2 data, the grey scale range is -0.5 – 10 MJy sr^{-1} . The numbers shown identify individual IR sources described in the text. (IRS1, IRS2, and IRS4 were classified as Class 0/I objects, and IRS3, IRS5, and IRS6 were classified as Class II sources in Paper I.)

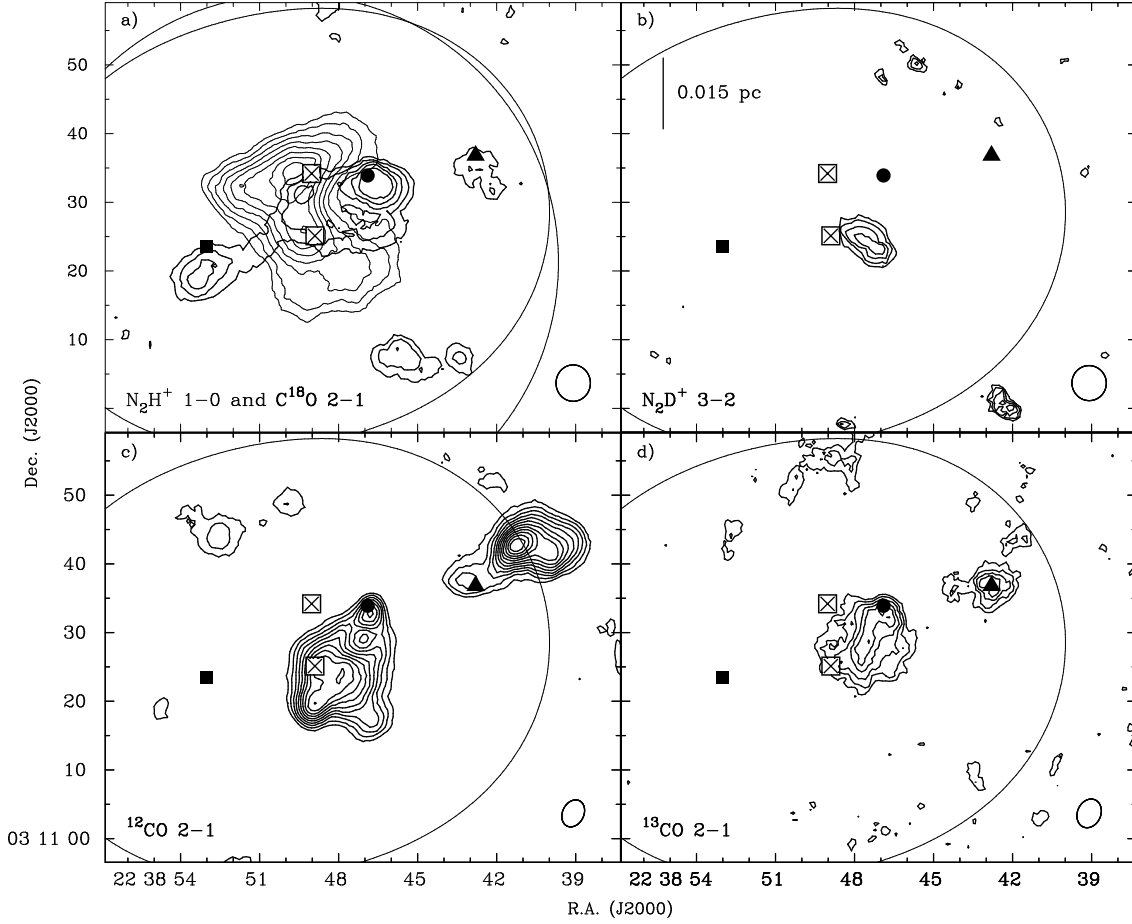


Fig. 8.— Integrated intensities of molecular transitions observed at SMA, found by determining the “zeroth-moment,” i.e., summing over channels with emission $> |2| \sigma$. Each contour set begins at the respective 2σ level and increases in steps of respective 1σ . In each panel, the ellipse to the lower right denotes the size and P.A. of the respective synthesized beam FWHM. In each panel, the large oval denotes the extent of the half-power sensitivity of the two-pointing mosaic, obtained from the continuum data obtained when the lines were observed. (The primary beam attenuation was corrected when these mosaics were made.) Various symbols are defined as in previous Figures. a) Integrated intensities of C^{18}O 2–1 (thick contours) where $1 \sigma \approx 0.5 \text{ K km s}^{-1}$. For comparison, the integrated intensities of N_2H^+ 1–0 from Figure 7a are also shown. (The outer large circle denotes the primary beam FWHM of the N_2H^+ data.) b) Integrated intensities of N_2D^+ 3–2 where $1 \sigma \approx 0.5 \text{ K km s}^{-1}$. (The contours just south of the half-power sensitivity oval are tracing amplified noise and not N_2D^+ emission.) c) Integrated intensities of ^{12}CO 2–1 where $1 \sigma \approx 7 \text{ K km s}^{-1}$. d) Integrated intensities of ^{13}CO 2–1 where $1 \sigma \approx 2 \text{ K km s}^{-1}$.

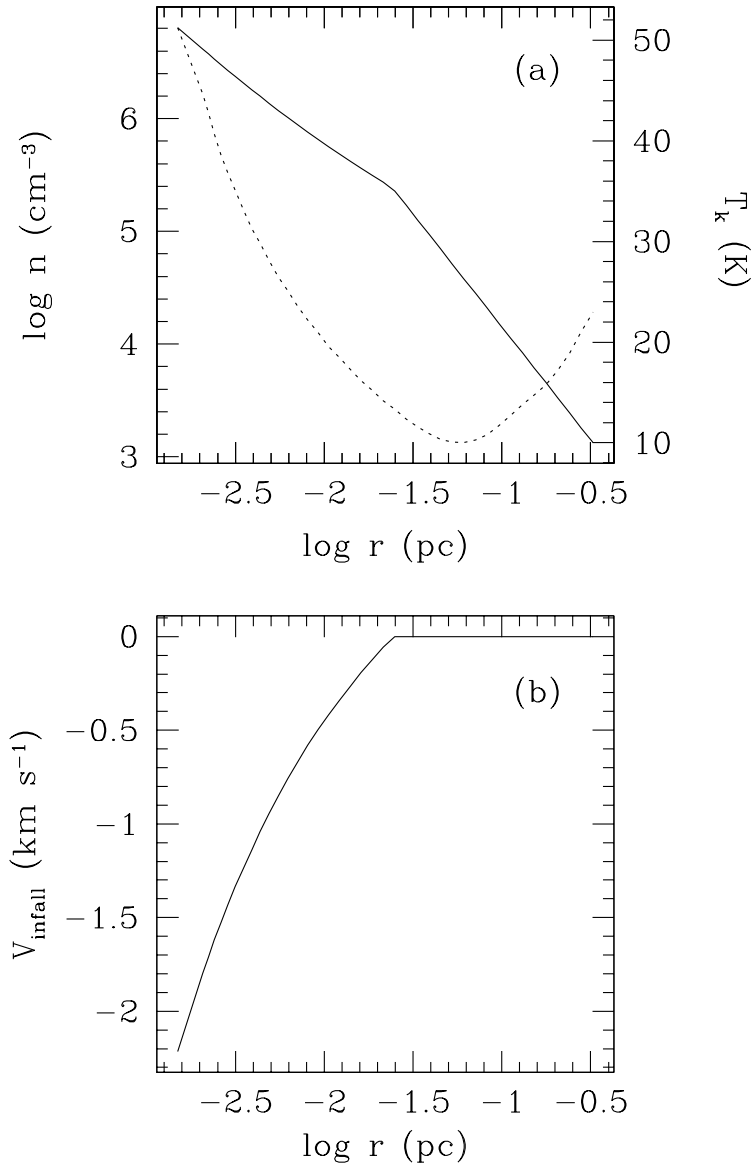


Fig. 9.— Density (a) and infall velocity (b) profiles of the best-fit inside-out collapse model of L1251B for the dust continuum observations at 450 μm and 850 μm . The infall radius is 5000 AU, equivalent to an infall timescale of 5×10^4 years. The kinetic temperature profile in (a) has been calculated by balancing the heating and cooling of gas from the dust temperature profile obtained from the dust continuum modeling (See Young et al. 2003 for details of the dust modeling process.) At small radii, the kinetic temperature is well coupled with the dust temperature, but at large radii, it is higher than the dust temperature mainly due to the photoelectric heating.

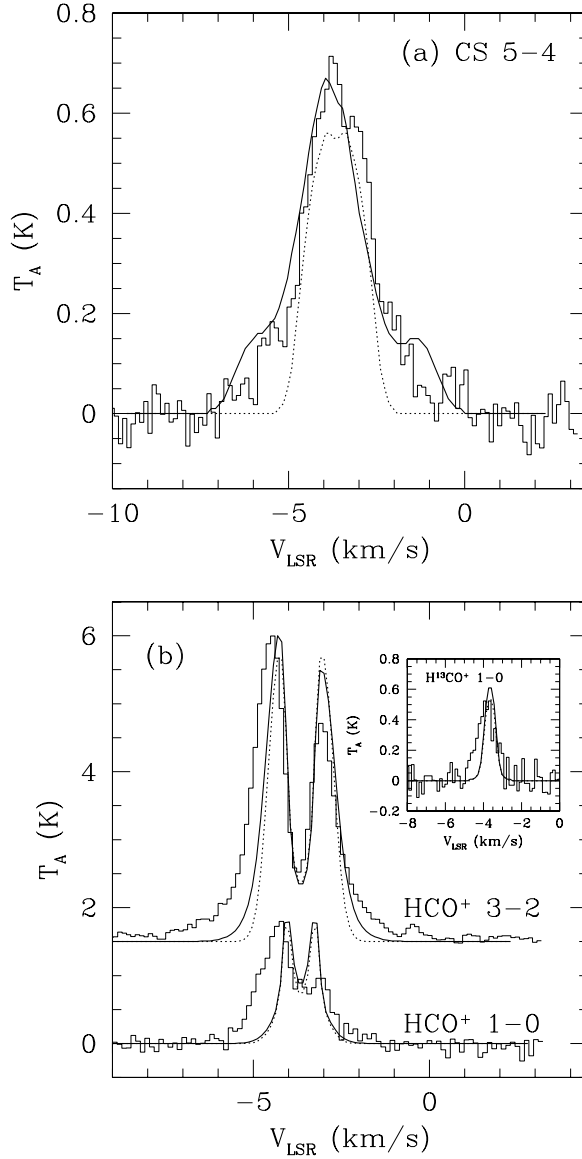


Fig. 10.— Comparisons between observations (histogram) and models with (solid line) and without (dotted line) the consideration of infall velocity profile in CS 5–4 (a) and HCO⁺ 3–2 and H¹³CO⁺ 1–0 (b). For the line radiative transfer calculations, physical conditions in Figure 9 have been used, and the abundance profiles were adopted from Fig. 18. For the H¹³CO⁺ abundance profile, the abundance ratio, $^{12}\text{C}/^{13}\text{C}=77$ was assumed, and the HCO⁺ abundance profile for HCO⁺ 3–2 has been reduced by a factor of 2 from the profile seen in Fig. 18. The infall velocity profile is important to produce the broad wings of CS 5–4, which traces very high densities. The line wings of HCO⁺ 3–2 and H¹³CO⁺ 1–0 may be also affected by outflow, which is not considered in this modeling.

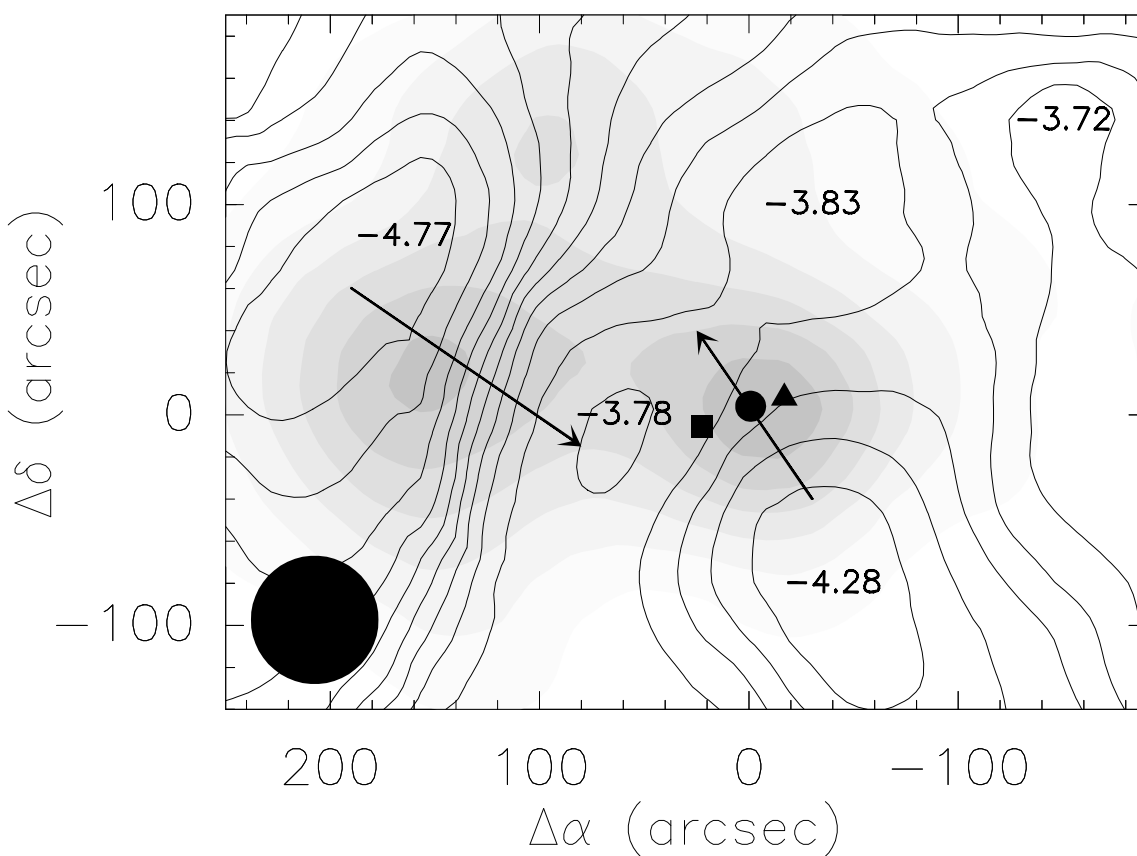


Fig. 11.— The centroid velocity distribution of HCN 1–0 as observed from FCRAO overlaid onto its integrated intensity map. Centroid velocities were calculated by fitting the hyperfine structure of HCN 1–0. The interval of contours is 0.1 km s^{-1} and numbers indicate local extrema of centroid velocity. The arrows indicate the directions of velocity gradients from blue to red. The uncertainty of fitting of the centroid velocity is less than 0.1 km s^{-1} .

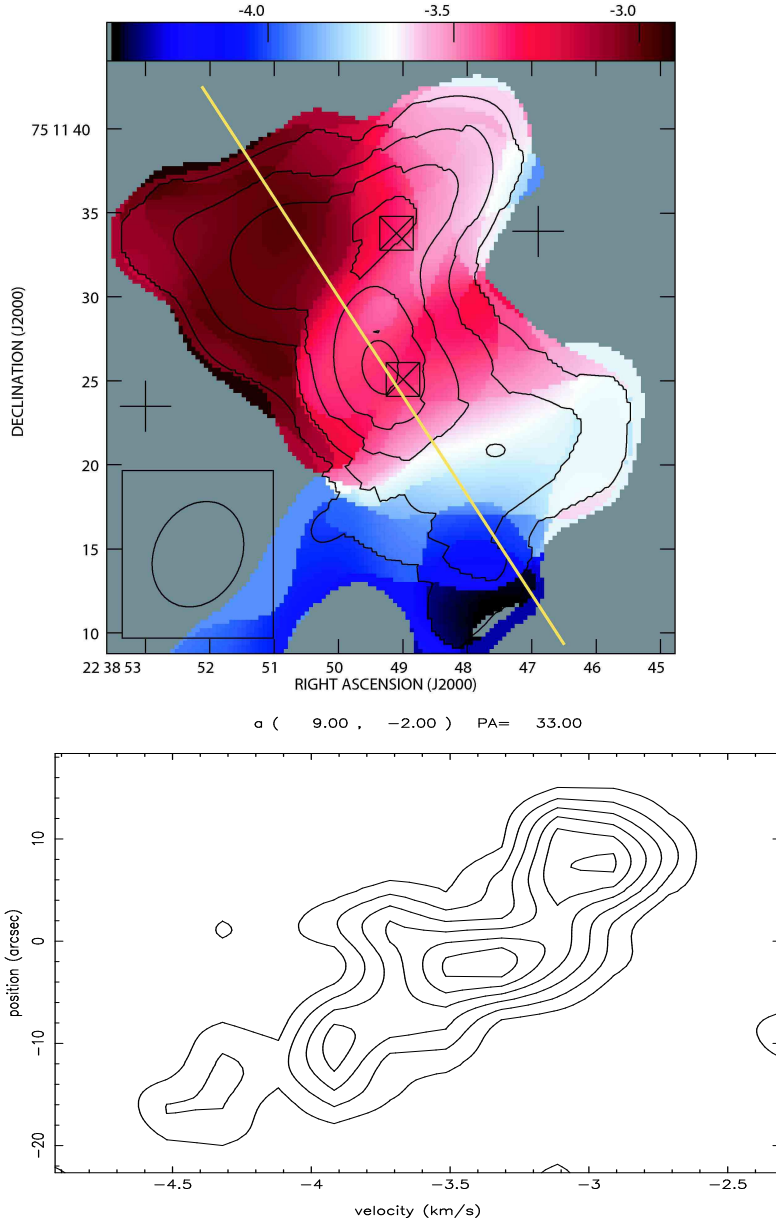


Fig. 12.— (a) The integrated intensity contours overlaid onto the mean centroid velocity image of the isolated component ($F=01-12$) of $N_2H^+ 1-0$ observed at the OVRO. The moments were calculated in channels with emission $> 2\sigma$. The contours begin at 3σ and increase in steps of 3σ , where 1σ is 1.5 K km s^{-1} . Crosses denote the positions of IRS1 and IRS2, and the square-X symbols indicate the positions of SMA-N and SMA-S. The ellipse to the lower left represents the synthesized beam of the $N_2H^+ 1-0$ observation. The overlaid line indicates the direction for the position-velocity diagram in (b). (b) The position-velocity diagram of the isolated component along the cut that centers at the emission peak, $(\Delta\alpha, \Delta\delta) = (9'', -2'')$ with P.A. = 33° . This cut is basically along the integrated intensity map elongated in the direction of northeast–southwest crossing the emission peak. For these figures, the isolated component has been shifted in velocity by 8.0 km s^{-1} . The contours begin at 2σ and increase in steps of 2σ , where 1σ is 0.25 K beam^{-1} .

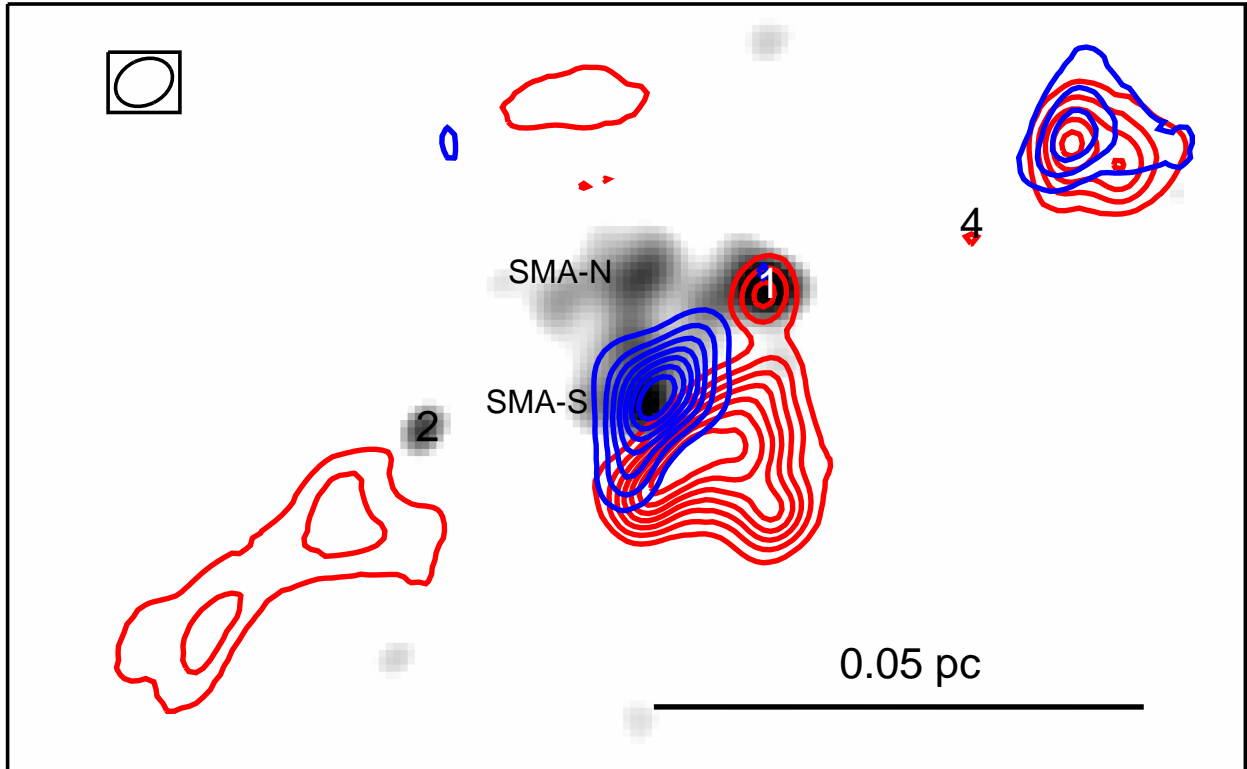


Fig. 13.— Integrated intensities of red- and blueshifted emission of ^{12}CO 2–1 overlaid onto the 1.3 mm continuum emission image observed at the SMA. Red and blue contours denote intensities calculated over “blue” and “red” velocity ranges, respectively. The same velocity ranges as in Figure 5 were used. Numbers indicate positions of IRS1, IRS2, and IRS4. Two starless condensations are named SMA-N and SMA-S. The ellipse to the upper left denotes the synthesized beam of the CO 2–1 observation. The contours begin at 4σ and increase in steps of 4σ , where $1\sigma = 2.14 \text{ K km s}^{-1}$. The grey scale range is $0.01 - 0.0275 \text{ Jy beam}^{-1}$.

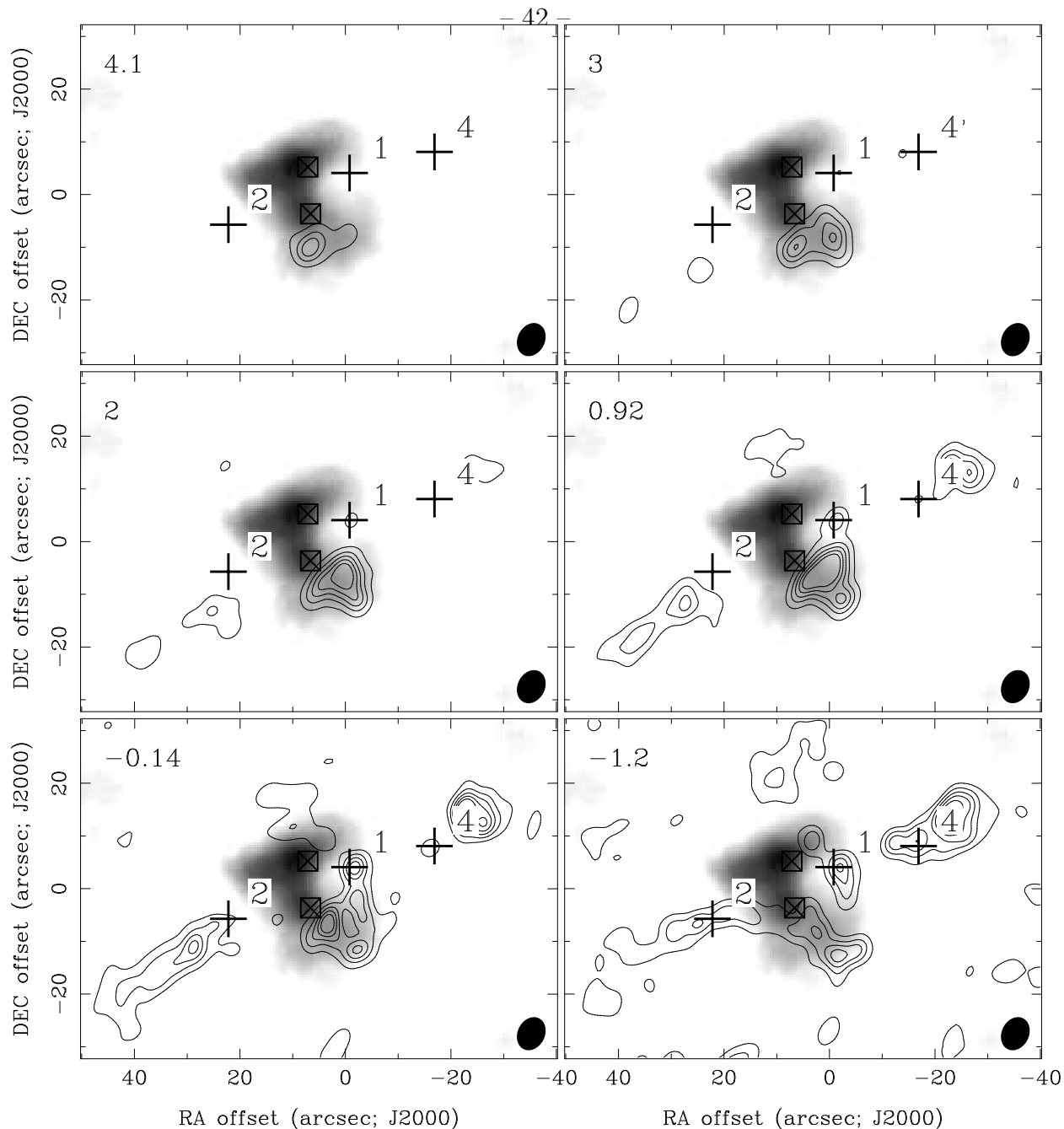


Fig. 14.— The channel map of redshifted emission of ^{12}CO 2-1 observed at the SMA overlaid onto the integrated intensity image of N_2H^+ 1-0 observed at the OVRO. The contours begin at 6σ and increase in steps of 9σ , where 1σ is 0.36 K . The grey scale range is 1.5 K km s^{-1} to 15 K km s^{-1} . Two square-X symbols indicate the positions of SMA-N and SMA-S, and crosses denote the positions of IRS1, IRS2, and IRS4. The ellipse to the lower right in each panel denotes the synthesized beam of the CO 2-1 observation.

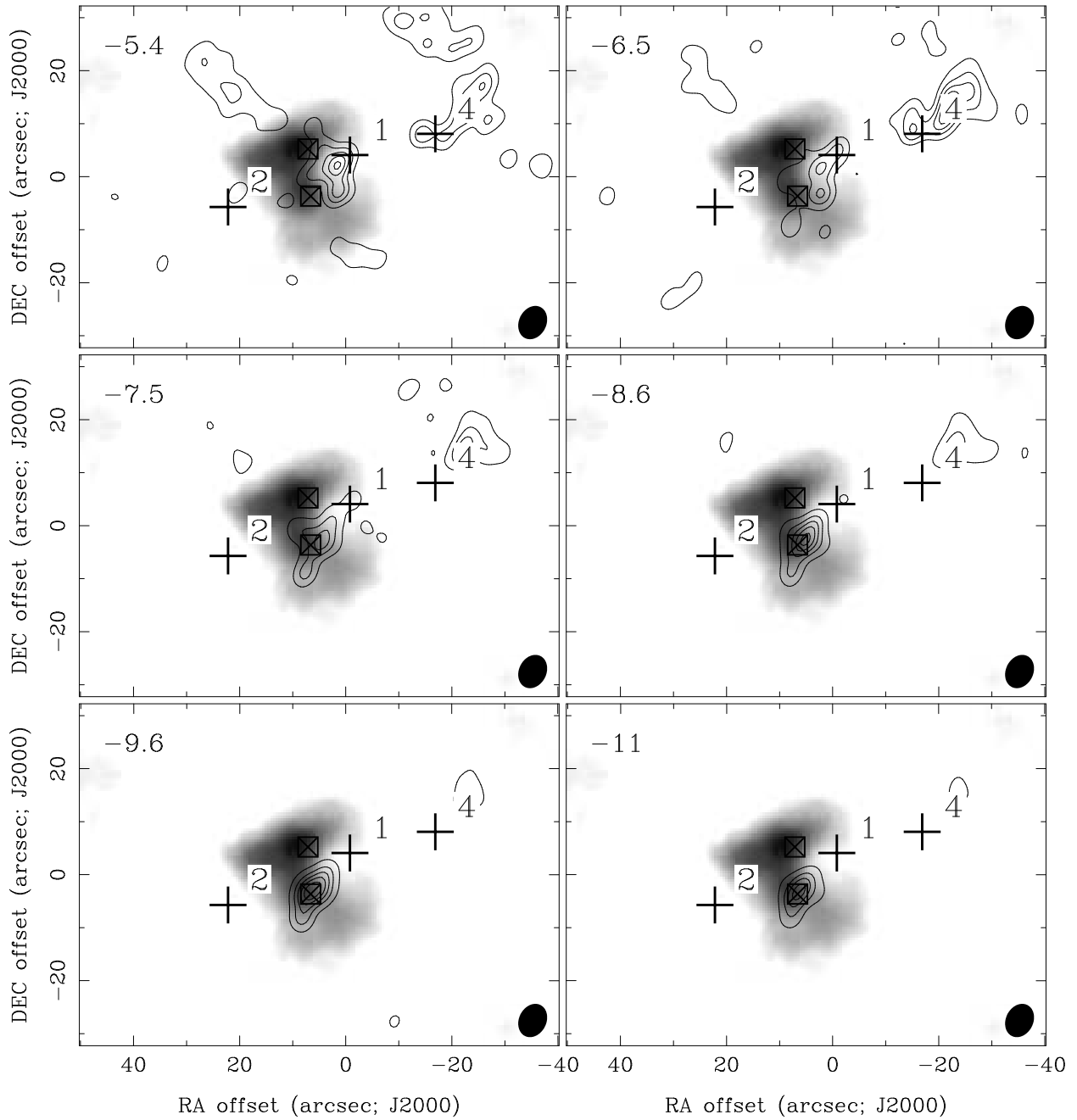


Fig. 15.— The channel map of blueshifted emission of ^{12}CO 2–1 observed at the SMA overlaid onto the integrated intensity image of N_2H^+ 1–0 observed at the OVRO. The contour levels and grey scale are the same as in Figure 14.

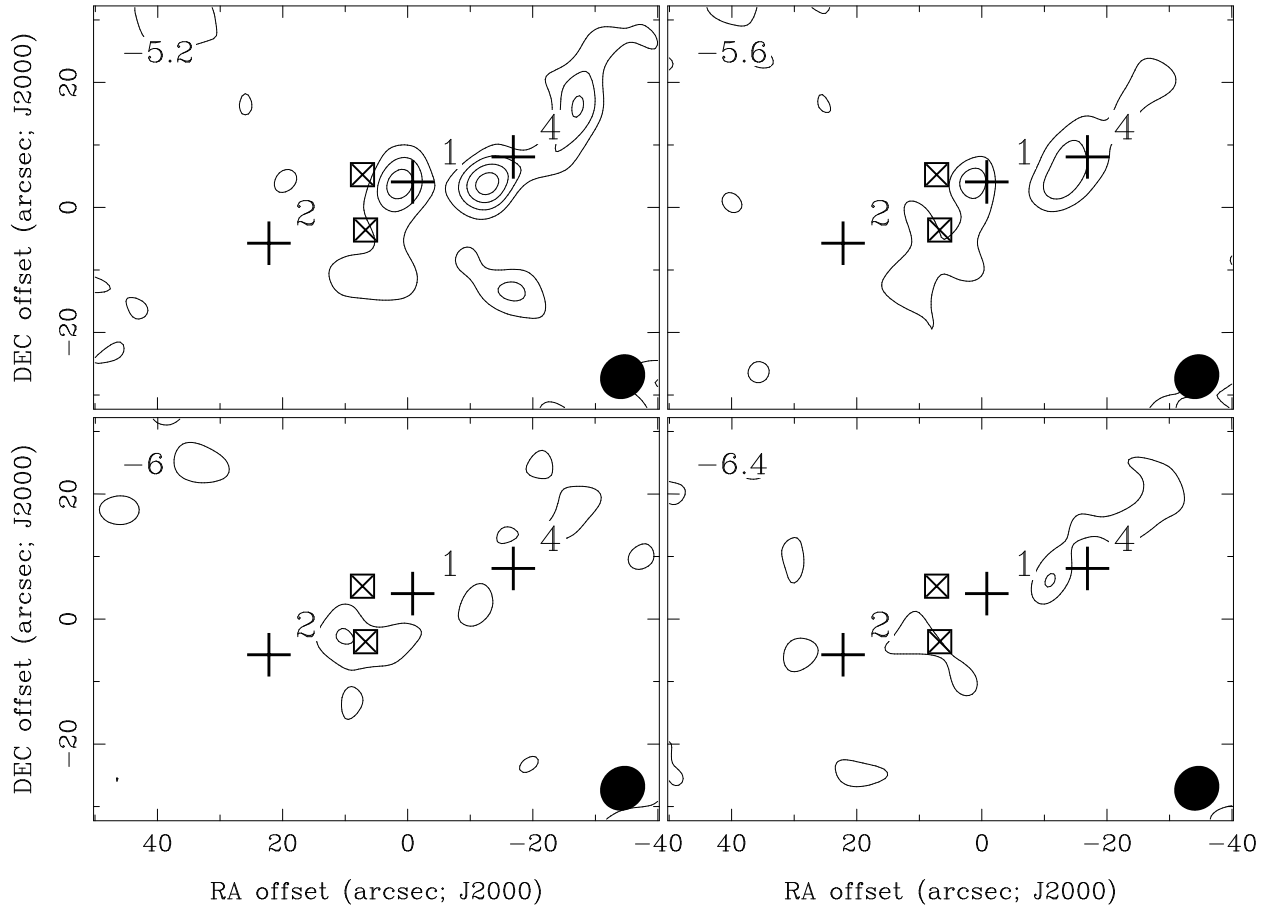


Fig. 16.— The channel map of blueshifted emission of HCO⁺ 1–0 observed at the OVRO. Symbols are the same as in Figure 14 and 15. The contours begin at 2 σ and increase in steps of 2 σ , where 1 σ = 0.22 K.

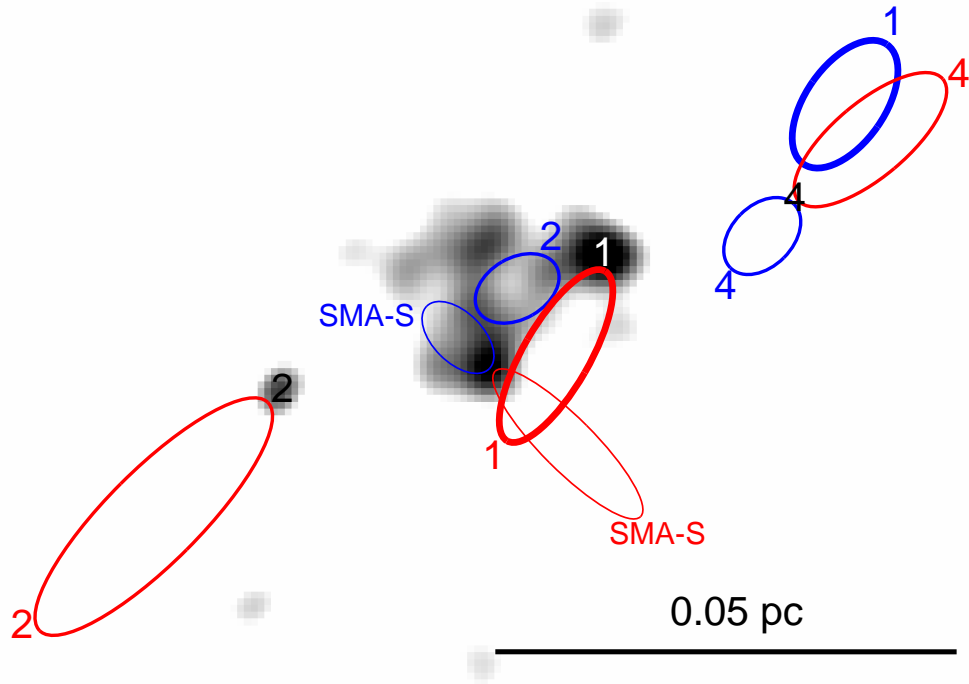


Fig. 17.— A possible explanation of the origin of each outflow. The grey image is the same as that in Figure 13. Black and white numbers denote the positions of IRS1, IRS2, and IRS4. Red and blue lobes describe the red and blue components each outflow identified in the channel maps of CO 2–1 and HCO⁺ 1–0 observed at the SMA and the OVRO, respectively. Red and blue numbers and texts indicate the red- and blueshifted lobes originated from their corresponding sources.

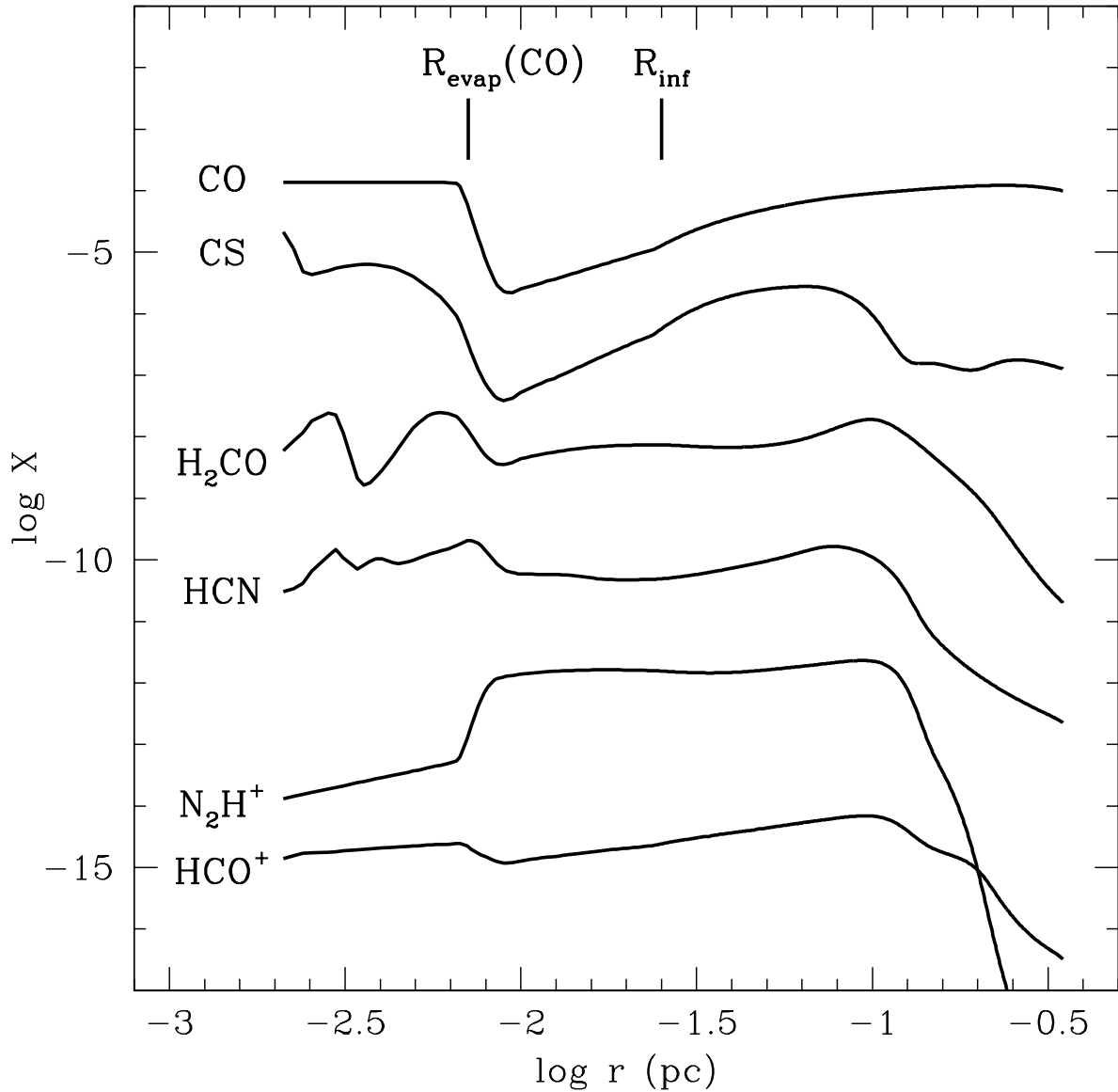


Fig. 18.— Abundance profiles of various molecules observed for this study. The profiles have been calculated using an evolutionary chemical model (Lee et al. 2004) defined on the basis of the physical parameters of L1251B. Two vertical lines indicate the infall radius of the inside-out collapse and the radius where CO starts to evaporate. Profiles are shifted up and down for easier comparisons, so the ordinate gives correct abundance of only CO. Abundances of CS and H₂CO are shifted up by 3.0 and 0.2 orders of magnitude respectively, while those of HCN, N₂H⁺, and HCO⁺ are shifted down by 1.0, 2.5, and 6.0 orders of magnitude respectively.